

# Npas1<sup>+</sup> Pallidal Neurons Target Striatal Projection Neurons

Kelly E. Glajch,<sup>1\*</sup> Daniel A. Kelter,<sup>1\*</sup> Daniel J. Hegeman,<sup>1\*</sup> Qiaoling Cui,<sup>1</sup> Harry S. Xenias,<sup>1</sup> Elizabeth C. Augustine,<sup>1</sup> Vivian M. Hernández,<sup>1</sup> Neha Verma,<sup>1</sup> Tina Y. Huang,<sup>1</sup> Minmin Luo,<sup>2,3</sup> Nicholas J. Justice,<sup>4</sup> and C. Savio Chan<sup>1</sup>

<sup>1</sup>Department of Physiology, Feinberg School of Medicine, Northwestern University, Chicago, Illinois 60611, <sup>2</sup>National Institute of Biological Sciences, Beijing 102206, China, <sup>3</sup>School of Life Sciences, Tsinghua University, Beijing 100084, China, and <sup>4</sup>Institute of Molecular Medicine, University of Texas, Houston, Texas 77030

Compelling evidence demonstrates that the external globus pallidus (GPe) plays a key role in processing sensorimotor information. An anatomical projection from the GPe to the dorsal striatum has been described for decades. However, the cellular target and functional impact of this projection remain unknown. Using cell-specific transgenic mice, modern monosynaptic tracing techniques, and optogenetics-based mapping, we discovered that GPe neurons provide inhibitory inputs to direct and indirect pathway striatal projection neurons (SPNs). Our results indicate that the GPe input to SPNs arises primarily from Npas1-expressing neurons and is strengthened in a chronic Parkinson's disease (PD) model. Alterations of the GPe-SPN input in a PD model argue for the critical position of this connection in regulating basal ganglia motor output and PD symptomatology. Finally, chemogenetic activation of Npas1-expressing GPe neurons suppresses motor output, arguing that strengthening of the GPe-SPN connection is maladaptive and may underlie the hypokinetic symptoms in PD.

**Key words:** 6-OHDA; arky pallidal neurons; extrinsic inhibition; Npas1-Cre; pallidostriatal projection

## Significance Statement

An anatomical projection from the pallidum to the striatum has been described for decades, but little is known about its connectivity pattern. The authors dissect the presynaptic and postsynaptic neurons involved in this projection, and show its cell-specific remodeling and strengthening in parkinsonian mice. Chemogenetic activation of Npas1<sup>+</sup> pallidal neurons that give rise to the principal pallidostriatal projection increases the time that the mice spend motionless. This argues that maladaptive strengthening of this connection underlies the paucity of volitional movements, which is a hallmark of Parkinson's disease.

## Introduction

The external globus pallidus (GPe) is involved in processing sensorimotor information (DeLong, 1971; Anderson and Horak,

1985; Mitchell et al., 1987; Jaeger et al., 1995; Kimura et al., 1996; Raz et al., 2000; Nambu et al., 2002; Arkadir et al., 2004; Turner and Anderson, 2005; Obeso et al., 2006; Kita, 2007; Tachibana et al., 2011; Jin et al., 2014; Dodson et al., 2015; Mallet et al., 2016; Yoshida and Tanaka, 2016), and alterations in GPe function have been directly linked to motor symptoms in disorders such as Parkinson's disease (PD; Bergman et al., 1998; Hauber, 1998; Vitek et al., 2004; Rajput et al., 2008; Johnson et al., 2012; Vitek et al., 2012; Abedi et al., 2013). Consistent with its role in sensorimotor function, a growing body of literature suggests that the GPe projects to all basal ganglia nuclei (Parent and Hazrati, 1995; Mink, 1996; Bolam et al., 2000; Kita, 2007; Mallet et al., 2012). These findings argue for a central position of the GPe in the basal ganglia circuitry (for review, see Hegeman et al., 2016).

A projection from the GPe to the dorsal striatum (dStr), the primary input center of the basal ganglia, was postulated over a century ago (Wilson, 1911, 1913), and its existence has since been confirmed in a variety of species (Nauta, 1979; Staines et al., 1981;

Received May 1, 2015; revised March 30, 2016; accepted April 3, 2016.

Author contributions: K.E.G., D.A.K., D.J.H., Q.C., H.S.X., E.C.A., V.M.H., and C.S.C. designed research; K.E.G., D.A.K., D.J.H., Q.C., H.S.X., E.C.A., V.M.H., T.Y.H., and C.S.C. performed research; M.L. and N.J.J. contributed unpublished reagents/analytic tools; K.E.G., D.A.K., D.J.H., Q.C., H.S.X., E.C.A., V.M.H., N.V., and C.S.C. analyzed data; K.E.G., D.J.H., and C.S.C. wrote the paper.

This work was supported by grants from the Parkinson's Disease Foundation and National Institutes of Health (NIH) Grant NS 041234 (to K.E.G.); NIH Grant NS 041234 (to H.S.X.); the China Ministry of Science and Technology Science Fund for Creative Research Group of China Grants 2012CB837701 and 2012YQ03026005, and National Natural Science Foundation of China Grant 91432114 (to M.L.); NIH Grant AG 036738 (to N.J.J.); and Northwestern Memorial Foundation Parkinson's Disease and Movement Disorders Advisory Council Grant, American Parkinson Disease Association, and NIH Grants NS 069777, NS 069777-S1, and NS 047085 (to C.S.C.). We thank Ellie Hong, Bonnie Erjavec, Jason Barraza, Yu Chen, Michael Fiske, and Thomas Madathany for their technical assistance; and members of the Chan laboratory for discussions. We also thank Eileen McIver and Dr. Mark Bevan for sharing their DREADD virus and experience with chemogenetic experiments. Finally, we thank Drs. Vandana Chinwalla and Sanza Kazadi from the Illinois Mathematics and Science Academy for their opportunity for the partnership with the SIR program.

\*K.E.G., D.A.K., and D.J.H. are co-first authors.

The authors declare no competing financial interests.

Correspondence should be addressed to C. Savio Chan, Department of Physiology, Feinberg School of Medicine, Northwestern University, 303 East Chicago Avenue, Chicago, IL 60611. E-mail: saviochan@gmail.com.

DOI:10.1523/JNEUROSCI.1720-15.2016

Copyright © 2016 the authors 0270-6474/16/365472-17\$15.00/0

Beckstead, 1983; Jayaraman, 1983; Staines and Fibiger, 1984; Fisher et al., 1985; Smith and Parent, 1986; Takada et al., 1986; Shu and Peterson, 1988; Walker et al., 1989; Kita and Kitai, 1991; Shinonaga et al., 1992; Rajakumar et al., 1994; Shammah-Lagnado et al., 1996; Spooren et al., 1996; Nambu and Llinás, 1997; Bevan et al., 1998; Kita et al., 1999; Sato et al., 2000; Kita and Kita, 2001; Mallet et al., 2012; Mastro et al., 2014; Abdi et al., 2015; Fujiyama et al., 2015; Saunders et al., 2016). However, very little is known about the identities of the GPe neurons that provide this input or the postsynaptic neurons they target. A major impediment to our understanding of the pallidostriatal pathway arises from the cellular complexity in the dStr and the GPe, as each of these nuclei comprises several types of neurons (Kita, 2007; Kreitzer, 2009; Tepper et al., 2010; Mallet et al., 2012; Gittis et al., 2014; Abdi et al., 2015; Dodson et al., 2015). Therefore, it is evident that we need a systematic analysis to map the connectivity between specific pallidostriatal inputs and identified postsynaptic target neurons. Similarly, the relevance of the pallidostriatal pathway to basal ganglia function and dysfunction remains to be established.

Taking advantage of recently developed cell- and circuit-specific tools, our study sought to delineate the connectivity patterns and physiological impacts of the distinct GPe inputs to dStr neurons and how these parameters are changed in a PD model. We found that GPe input to the dStr targeted striatal spiny projection neurons (SPNs) and interneurons (INTs). The GPe-SPN input arose primarily from Npas1-expressing ( $Npas1^{+}$ ) GPe neurons. Furthermore, the pallidostriatal input to SPNs was enhanced in a chronic 6-OHDA lesion model of PD. These findings argue for the critical position of the GPe-SPN connection in regulating basal ganglia motor output and PD symptomatology.

## Materials and Methods

**Animals.** All experiments detailed were performed in accord with the Institutional Animal Care and Use Committees at Northwestern University, the National Institute of Biological Sciences, and the Ethics Committee of Wuhan Institute of Physics and Mathematics, Chinese Academy of Sciences, and are in compliance with the National Institutes of Health *Guide to the Care and Use of Laboratory Animals*.

Experiments were conducted with *Chat<sup>Cre</sup>*, *Drd1a<sup>Cre</sup>*, *Drd1a<sup>eGFP</sup>*, *Drd1a<sup>tdTomato</sup>*, *Drd2<sup>Cre</sup>*, *Drd2<sup>eGFP</sup>*, *Npas1<sup>Cre-2A-tdTomato</sup>*, *Pvalb<sup>Cre</sup>*, *R26<sup>LSL-ChR2(H134R)-eYFP</sup>*, and *R26<sup>LSL-tdTomato</sup>* mice. The *Drd1a<sup>tdTomato</sup>* mouse was a gift from Dr. Nicole Calakos (Duke University, Durham, NC; Shuen et al., 2008). The *Npas1<sup>Cre-2A-tdTomato</sup>* mouse (Hernández et al., 2015) was generated by the Northwestern Transgenic and Targeted Mutagenesis Laboratory (Hernández et al., 2015). All other mice were obtained from the MMRRC (Gong et al., 2003; Gerfen et al., 2013) or The Jackson Laboratory. Mice for all experiments were maintained on a C57BL/6 background. Both male and female hemizygous or heterozygous mice were used in this study.

**Drugs.** CGP55845, R-CPP, NBQX disodium salt, picrotoxin, QX314-Cl, RuBi-GABA, SR95531, and TTX were obtained from Abcam.  $K_2SO_4$  and  $Na_2$ -GTP were from ICN Biomedicals and Roche, respectively. All other reagents were obtained from Sigma-Aldrich. Drugs were dissolved as stock solutions in water, DMSO, or artificial CSF (aCSF), and were aliquoted and frozen at  $-30^{\circ}C$  before use. Each of the drugs was diluted to the appropriate concentrations by adding it to the perfusate immediately before the experiment. The final concentration of DMSO in the perfusate was  $\leq 0.1\%$ .

**Chronic dopamine depletion.** A unilateral lesion of the nigrostriatal system was produced by 6-hydroxydopamine (6-OHDA) injection into the medial forebrain bundle (MFB; Chan et al., 2011; Fan et al., 2012; Glajch et al., 2012; Heuer et al., 2012). Mice at postnatal days 28–35 were anesthetized with isoflurane and immobilized on a stereotaxic frame (David Kopf Instruments). A small craniotomy ( $\sim 1$  mm diameter) was made with a dental drill (Osada) for injection into the MFB [anteroposterior (AP)  $-0.7$  mm and

mediolateral (ML)  $+1.1$  mm from bregma; dorsoventral (DV)  $-4.8$  mm from the dura]. 6-OHDA ( $2.5 \mu g/\mu l$ ) was dissolved in  $0.9\%$  w/v NaCl with  $0.1\%$  w/v ascorbic acid, and  $1 \mu l$  was injected using a calibrated glass micropipette (VWR) at a rate of  $0.3$ – $0.5 \mu l/min$ . The micropipette was left *in situ* for 5–10 min postinjection to maximize tissue retention of 6-OHDA and to decrease capillary spread upon pipette withdrawal. At 3 weeks after 6-OHDA injection, the cylinder test was used to quantify impairment in forelimb usage as an assessment of the degree of dopamine depletion (Schallert et al., 2000). All initial contacts made by each forepaw on the wall of a clear glass cylinder (9 cm diameter) during spontaneous exploratory behavior were counted during a 5 min period. Mice with  $<20$  total touches were excluded because of an incomplete lesion. Asymmetry of the forelimb usage was expressed as the “limb-use asymmetry ratio” [independent contralateral forepaw placement relative to that of the ipsilateral (to the lesion) forepaw against the wall of the chamber during rearing and vertical or lateral explorations; Glajch et al., 2012]. Electrophysiological experiments were performed 4–6 weeks after 6-OHDA injection.

**Viruses and injection procedures.** Adeno-associated viruses (AAVs) were obtained from the University Pennsylvania Viral Vector Core and the University of North Carolina at Chapel Hill Gene Therapy Center Vector Core. Constitutive, pan-neuronal hSyn-hChR2(H134R)-enhanced yellow fluorescent protein (eYFP;  $3.6 \times 10^{13}$  genomic copies/ml) and Cre-inducible expression (CreOn) EF1 $\alpha$ -DIO-hChR2(H134R)-eYFP ( $0.7 \times 10^{13}$  genomic copies/ml) AAVs serotype 9 were diluted in sterile PBS to their final titer, and were injected into the GPe (135 nl at AP  $-0.46$  mm, ML  $+1.97$  mm, and DV  $-4.0$  mm from bregma) alone or concomitantly with MFB 6-OHDA injections (see above). CreOn hSyn-DIO-hm3Dq-mcherry ( $5.7 \times 10^{12}$  genomic copies/ml) AAV serotype 8 was not further diluted and was injected bilaterally into the GPe (135 nl at AP  $-0.35$  mm, ML  $\pm 2.2$  mm, DV  $-3.6$  mm, and  $-4.1$  mm from bregma). Viruses and procedures for monosynaptic retrograde labeling have been described previously (Guo et al., 2015).

**Immunohistochemistry.** Mice with an age range of postnatal day 55–80 were anesthetized deeply with a ketamine–xylazine mixture and perfused transcardially first with PBS or  $0.9\%$  saline solution, followed by fixative containing  $4\%$  paraformaldehyde, pH 7.4. Tissue was then postfixed in the same fixative for 1 h at  $4^{\circ}C$ . Tissue blocks containing the dStr and the GPe were sectioned using a vibrating microtome (Leica Instruments) at a thickness of  $50$ – $70 \mu m$ . Floating sections were blocked with  $2.5$ – $10\%$  (v/v) normal goat or donkey serum (Invitrogen) and  $0.1\%$  (v/v) Triton X-100 in PBS for 30–60 min, and subsequently were incubated with primary antibodies in the same solution for 16–24 h at  $4^{\circ}C$ . The primary antibodies used in this study include the following: GFP (1:1000; Abcam), HuCD (1:1000; Life Technologies), parvalbumin (1:500; Synaptic Systems), RFP (1:500; Abcam), and vesicular GABA transporter (VGAT; 1:500; Synaptic Systems). After washes in PBS, the sections were incubated with Alexa Fluor-conjugated IgG antibody (Invitrogen) at room temperature for 2 h. The sections were then washed, mounted, and coverslipped. Immunoreactivity was examined on a laser-scanning confocal microscope (Olympus Optical). For axonal density measurements, a region of interest (ROI) was selected at a comparable position for each striatal section. Background fluorescence was then subtracted from each pixel in the ROI. Mean pixel intensities were subsequently measured and normalized to the GPe fluorescence level in each mouse. For rabies virus-tracing experiments, image stacks of the GPe were acquired at  $25\times$  on a laser-scanning confocal microscope (Olympus Optical) and were then analyzed by two individuals, including one who was blinded to the experimental conditions. The number of retrogradely labeled cells within the GPe and their expression of parvalbumin were determined by visual inspection of all three orthogonal planes in Fiji (Schindelin et al., 2012).

**Fluorescence-activated cell sorting and quantitative PCR.** Experimental procedures and data processing for fluorescence-activated cell sorting (FACS) and quantitative PCR (qPCR) were similar to the analysis in our previous studies (Sheets et al., 2011; Plotkin et al., 2014). *Ex vivo* slices were prepared as described above, striata were microdissected, and single-cell suspensions were generated using a combination of enzymatic and mechanical dissociation procedures. Direct-pathway SPNs (dSPNs) and indirect-pathway SPNs (iSPNs) were purified using FACS on a cell sorter (BD Biosciences), based on tdTomato or enhance green fluores-

**Table 1. Primer sequences and weighting factors of reference genes**

Full target gene names	Gene name	Upper primer	Lower primer	Weighting Factor
GABA <sub>A</sub> receptor $\alpha$ 1-subunit	<i>Gabra1</i>	ACCAGTTTCGGACCACTTCAGAC	TGTTAGCCGGAGCACTGTCAT	
GABA <sub>A</sub> receptor $\alpha$ 2-subunit	<i>Gabra2</i>	GTGTCATTCTGGCTGAACAGAG	AGTCCATGGCAGTGGCATAA	
GABA <sub>A</sub> receptor $\alpha$ 4-subunit	<i>Gabra4</i>	GGGGTCCTGTACAGAAAGTGAA	AGGGGTCCAAACTTTGGTGA	
GABA <sub>A</sub> receptor $\beta$ 1-subunit	<i>Gabrb1</i>	GAAGATCCCTTACGTCAAAGCG	TTTCTGAGGGCTTTTCCGA	
GABA <sub>A</sub> receptor $\beta$ 2-subunit	<i>Gabrb2</i>	GACAATCGAGTCACAGGAGT	GGCATGTATGTCTGCAGGAT	
GABA <sub>A</sub> receptor $\beta$ 3-subunit	<i>Gabrb3</i>	ACGGTCGACAAGCTGTTGAA	GAGGTTGAGAGGGATCCCAGAATA	
GABA <sub>A</sub> receptor $\gamma$ 2-subunit	<i>Gabrg2</i>	GAGTTCGCCAATACATGGAG	TAGAGCCGATAGCAGGAGCA	
GABA <sub>A</sub> receptor $\gamma$ 3-subunit	<i>Gabrg3</i>	ACAGTCGCCTTCGATTCAAC	CACCTGCTGATTGATAGTGAGCC	
GABA <sub>A</sub> receptor $\delta$ -subunit	<i>Gabrd</i>	GCTGTACACATACCACGTGA	CAGGCTCGTCTTAGAGCAA	
Full reference gene names				
Glyceraldehyde-3-phosphate dehydrogenase	<i>Gapdh</i>	CATTTCAGTGGCAAAGTGG	GAATTTGCCGTGAGTGGAGT	0.3216
Cytochrome c-1	<i>Cyc1</i>	CATGAAGCGGCATAAGTGGT	GAGGGCTGAAGGAAGATCAGAA	0.2088
Succinate dehydrogenase complex, subunit A, flavoprotein (Fp)	<i>Sdha</i>	TACAAGGGACAGGTGCTGAA	GCCAAAGACTACAAGGTCCAAG	0.1531
H2A histone family, member Z	<i>H2afz</i>	AGTTGGCAGGAATGCGT	TCTTCCCGATCAGCGATTG	0.1122
ATP synthase, H <sup>+</sup> transporting mitochondrial F1 complex, $\beta$ subunit	<i>Atp5b</i>	GGCACAATGCAGGAAGGAT	ATGCCCACTCAGCAATAGC	0.0920
Ubiquitin carboxy-terminal hydrolase L1	<i>Uchl1</i>	AAGCAGACCATCGGAACTC	ACAGCTTCCGTTTCAGAC	0.0863

cent protein (eGFP) expression. Dead cells were excluded based on the DAPI or propidium iodide labeling. Approximately 10,000 cells from each mouse were collected, lysed using RealTime ready Cell Lysis Buffer (Roche), stored at  $-80^{\circ}\text{C}$ , and used for qPCR analysis. Immediately following total RNA isolation using the RNeasy Micro Kit (Qiagen), first-strand cDNA synthesis was performed using cDNA Supermix (Quanta Biosciences). cDNAs were then frozen at  $-20^{\circ}\text{C}$  until used. Desalted primers were custom synthesized (Invitrogen) and intron spanning whenever possible (Table 1). qPCRs were run in triplicate using Fast SYBR Green Mastermix (Applied Biosystems) on a qPCR instrument (Roche Applied Science). Negative controls for contamination from exogenous and genomic DNA were run for every gene target. The cycling protocol consisted of  $95^{\circ}\text{C}$  for 5 min followed by 45 cycles at  $95^{\circ}\text{C}$  for 10 s,  $60^{\circ}\text{C}$  for 10 s, and  $72^{\circ}\text{C}$  for 10 s. The PCR cycle threshold ( $C_T$ ) values were determined by the maxima of the second derivative of the fluorescence response curves. Melting curves were performed to verify the amplification of single PCR products. A weighted  $C_T$  (Table 1) was calculated from seven reference genes (*Atp5b*, *Cyc1*, *Eif4a2*, *Gapdh*, *H2afz*, *Sdha*, and *Uchl1*) for each cell sample based on their expression stability for normalization (Chan et al., 2012; Fan et al., 2012; Plotkin et al., 2013, 2014). The mRNA levels in each group of samples were characterized by their median values. Quantification of transcript expression changes was performed using the  $\Delta\Delta C_T$  method. Results were presented as fold changes relative to the median of their respective naïve controls.

**Visualized recording in ex vivo brain slices.** Mice in the age range postnatal day 55–90 were anesthetized with a ketamine-xylazine mixture and perfused transcardially with ice-cold aCSF containing the following (in mM): 125 NaCl, 2.5 KCl, 1.25  $\text{NaH}_2\text{PO}_4$ , 2.0  $\text{CaCl}_2$ , 1.0  $\text{MgCl}_2$ , 25  $\text{NaHCO}_3$ , and 12.5 glucose, bubbled continuously with carbogen (95%  $\text{O}_2$  and 5%  $\text{CO}_2$ ). The brains were rapidly removed, glued to the stage of a vibrating microtome (Leica Instrument), and immersed in ice-cold aCSF. Parasagittal slices containing the dStr and the GPe were cut at a thickness of 240  $\mu\text{m}$  and transferred to a holding chamber where they were submerged in aCSF at  $35^{\circ}\text{C}$  for 30 min and returned to room temperature for recording. Slices were then transferred to a small-volume ( $\sim 0.5$  ml) Delrin recording chamber that was mounted on a fixed-stage, upright microscope (Olympus Optical). Neurons were visualized using differential interference contrast optics (Olympus Optical), illuminated at 735 nm (Thorlabs), and imaged with a 60 $\times$  water-immersion objective (Olympus Optical) and a CCD camera (QImaging). SPNs and INTs in the sensorimotor region of the dStr were targeted in this study (McGeorge and Faull, 1989). SPNs were identified by somatic eGFP or tdTomato fluorescence examined under epifluorescence microscopy with a daylight (6500 K) LED (Thorlabs) and an appropriate filter cube (Semrock) to identify pathway-specific SPNs (i.e., dSPNs and iSPNs) from *Drd1a*- and *Drd2*-BAC transgenic mice (Gong et al., 2003; Shuen et al.,

2008; Chan et al., 2012). Additionally, SPNs were identified based on their membrane properties measured with a high-chloride internal solution (see below). Specifically, the membrane capacitance and membrane resistance of each cell were measured immediately after break-in using a monoexponential curve fitting of the transient current response to a +10 mV, 100 ms step from  $-80$  mV in pClamp10 (Molecular Devices). Cells with a membrane capacitance of typically  $>90$  pF and a membrane resistance of 150–400 M $\Omega$  were classified as SPNs. In a subset of recordings, Alexa Fluor 594 hydrazide (10–100  $\mu\text{M}$ ; Invitrogen) was included in the pipette solution to confirm the identity of SPNs by visualizing the presence of spine-dense dendrites. INTs were classified as cells with aspiny dendrites, membrane capacitances  $<90$  pF, and membrane resistances  $<150$  or  $>400$  M $\Omega$ . Fast-spiking interneurons were identified by their somatic tdTomato fluorescence signal in the *Pvalb*<sup>Cre</sup>;R26<sup>LSL-tdTomato</sup> mice. For GPe recordings in *Npas1*<sup>Cre-2A-tdTomato</sup> and *Pvalb*<sup>Cre</sup>;R26<sup>LSL-tdTomato</sup> mice, the neuron identity and Cre recombinase expression were determined by the somatic tdTomato fluorescence signal.

Recordings were made at room temperature (20–22 $^{\circ}\text{C}$ ) with patch electrodes fabricated from capillary glass (Sutter Instrument) pulled on a Flaming-Brown puller (Sutter Instrument) and fire polished with a microforge (Narishige) immediately before use. Pipette resistance was typically  $\sim 2$ –4 M $\Omega$ . For the dStr voltage-clamp recordings, a high-chloride internal solution was used. The high-chloride internal solution contained the following (in mM): 120 CsCl, 10  $\text{Na}_2$  phosphocreatine, 5 HEPES, 5 tetraethylammonium-Cl, 2  $\text{Mg}_2\text{ATP}$ , 1 QX314-Cl, 0.5  $\text{Na}_3\text{GTP}$ , 0.25 EGTA, and 0.2% (w/v) biocytin, with pH adjusted to 7.25–7.30 with CsOH. Alexa Fluor 594 hydrazide (10–100  $\mu\text{M}$ ) was also included in a subset of the recordings for morphological identification of dStr neurons. For the subthalamic nucleus (STN) recordings, a low-chloride internal solution was used. The low-chloride internal solution contained the following (in mM): 125 CsMeSO<sub>3</sub>, 10  $\text{Na}_2$  phosphocreatine, 5 HEPES, 5 tetraethylammonium-Cl, 2  $\text{Mg}_2\text{ATP}$ , 1 QX314-Cl, 0.5  $\text{Na}_3\text{GTP}$ , 0.25 EGTA, and 0.2% (w/v) biocytin, with pH adjusted to 7.25–7.30 with CsOH. For current-clamp recordings, the internal solution consisted of the following (in mM): 135 KMeSO<sub>4</sub>, 10  $\text{Na}_2$  phosphocreatine, 5 KCl, 5 EGTA, 5 HEPES, 2  $\text{Mg}_2\text{ATP}$ , 0.5  $\text{CaCl}_2$ , and 0.5  $\text{Na}_3\text{GTP}$ , with pH adjusted to 7.25–7.30 with KOH. The liquid junction potential for this internal solution was  $\sim 7$  mV and was not corrected. Photocurrent recordings in GPe neurons were collected with either the high-chloride voltage-clamp internal solution or the current-clamp internal solution. All internal solutions had an osmolarity of  $\sim 300$  mOsm/L. Somatic whole-cell patch-clamp recordings were obtained with an amplifier (Molecular Devices). The signal for voltage-clamp recordings was filtered at 1 kHz and digitized at 10 kHz with a digitizer (Molecular Devices). For current-clamp recordings, the amplifier bridge



circuit was adjusted to compensate for electrode resistance and was subsequently monitored. Stimulus generation and data acquisition were performed using pClamp10.

For optogenetic and GABA uncaging experiments, blue (peak, 450 nm) excitation wavelength from two daylight (6500 K) LEDs (Thorlabs) was delivered to the tissue slice from both the 60× water-immersion objective and the 0.9 numerical aperture air condenser with the aid of 520 nm dichroic beamsplitters (Semrock). The field of illumination is  $\sim 500$ – $700\ \mu\text{m}$  in diameter. The duration for all light pulses was 2 ms for optogenetic experiments and 10 ms for GABA-uncaging experiments. All recordings were made in the presence of *R*-CPP (10  $\mu\text{M}$ ) and NBQX (5  $\mu\text{M}$ ) to prevent the confounding effects of incidental activation of glutamatergic inputs.

Off-line data analyses and curve fitting were performed with MATLAB8 (MathWorks). A given event was considered a successful optogenetically driven monosynaptic response only if the amplitude exceeded four times the SD of the noise level in the inward direction and the response onset occurred within 2–8 ms after the light pulse for the dStr recordings; for the subthalamic nucleus recordings using terminal field stimulation, this parameter was 0–6 ms, which was applied to outward currents. Only cells for which this success rate was  $>25\%$  were deemed to be bona fide “responding” cells; all cells with success rates  $\leq 25\%$  were considered to be “nonresponding” cells. Rise times of 10–90% and decay times of 5–95% are used throughout. All decay measurements were performed on the last event in a given stimulus series. In experiments in which direct comparisons of IPSCs were made between neuron pairs, data were excluded if the series resistance of the patch pipette differed by  $>20\%$  between the two recordings. Paired-pulse ratios (PPRs) were calculated by dividing the averaged IPSC<sub>2</sub> amplitude by the averaged IPSC<sub>1</sub> amplitude.

**Anatomical analysis of GPe-SPN contacts.** To visualize the somatodendritic morphology of SPNs, Alexa Fluor 594 hydrazide (100  $\mu\text{M}$ ) was loaded into the cells via the patch pipette. Following the establishment of a whole-cell recording (see above), eYFP and Alexa Fluor 594 were excited using a 488 nm laser (Coherent) and 561 nm laser (Coherent), respectively. Confocal stacks of eYFP and Alexa Fluor 594 signals were acquired with a spinning-disk unit (Yokogawa) and an electron-multiplying CCD camera (Photometrics). Instrument control and data acquisition were performed using SlideBook6 (Intelligent Imaging Innovations). To determine the putative contacts formed between GPe axons and SPN dendrites, image stacks were visually inspected off-line in Fiji by an individual who was blinded to the cell type and treatment conditions. Synaptic contacts were deemed to be bona fide only if GPe axons and SPN dendrites were in close apposition in all *x*-( $\leq 0.2\ \mu\text{m}$ ), *y*-( $\leq 0.2\ \mu\text{m}$ ), and *z*-( $\leq 0.6\ \mu\text{m}$ ) planes. Euclidean distances between the contacts and the center of the cell body were measured. Clustering analysis of GPe-SPN contacts was performed in MATLAB8 using a *k*-means clustering algorithm.

**Behavior.** The assessment of motor behavior was accomplished using an automated home cage scoring system (Metris; Van de Weerd et al., 2001). Behavioral testing was performed between 3:30 P.M. and 6:30 P.M. under dim light (60 lux). Male control *Npas1-Cre* mice and DREADD hM3Dq-infected *Npas1-Cre* mice were repeatedly tested for 4 consecutive weeks [acclimation, baseline, clozapine *N*-oxide (CNO), and vehicle] at 1 week intervals. The control group of mice included naïve *Npas1-Cre* mice and sham-injected *Npas1-Cre* mice. The acclimation trial for the mice took place over postnatal days 49–58. The mice received no systemic drug or saline vehicle injection in acclimation and baseline trials. For the CNO trial, the mice were given an intraperitoneal injection of CNO at 3 mg/kg 10 min before behavioral assessment. For the vehicle trial, the mice were given an intraperitoneal injection of saline only. Each behavioral trial was 20 min. The bottoms of the behavior cages were cleaned with 70% ethanol, and new bedding was added before the testing of each mouse. The “time spent motionless” was defined as periods when the mouse was in a sitting or lying position with the absence of movement for  $>250$  ms. Similar analyses were performed in a separate cohort (postnatal day 55–97) of naïve *Npas1-Cre* mice ( $n = 14$ ) and naïve wild-type C57BL/6 mice ( $n = 19$ ) for only a single trial. Durations of locomotion ( $p = 0.4775$ ), climbing ( $p = 0.4997$ ), rearing ( $p = 0.8128$ ), and motionlessness ( $p = 0.2627$ ) were not different between the groups.

**Statistical analyses.** Statistical analyses were performed with MATLAB8 and Prism6 (GraphPad). Sample size (*n* value) is defined by the number of observations (i.e., cells, cell-pairs, synaptic contacts, ROIs, sections, or mice). No statistical method was used to predetermine sample size. Data in the main text are presented as median values  $\pm$  median absolute deviations as measures of central tendency and statistical dispersion, respectively. Box plots are used for graphic representation of population data (Krzywinski and Altman, 2014; Streit and Gehlenborg, 2014). The central line represents the median, the box edges represent the interquartile ranges, and the whiskers represent 10–90th percentiles. Normal distributions of data were not assumed. Comparisons for unrelated samples were performed using a Mann–Whitney *U* test at a significance level ( $\alpha$ ) of 0.05. The Wilcoxon signed rank test was used for pairwise comparisons for related samples with a threshold ( $\alpha$ ) of 0.05 for significance. The Fisher’s exact test was used for categorical data with a threshold ( $\alpha$ ) of 0.05 for significance. Unless  $<0.0001$ , exact *p* values (two-tailed) are reported.

## Results

### GPe axons target projection neurons and interneurons in the dStr

To examine the cellular connectivity between GPe and striatal neurons, optogenetics was used in conjunction with whole-cell patch-clamp recording in adult *ex vivo* mouse brain slices (Fig. 1*a*). Delivery of an AAV expressing a channelrhodopsin-2 (ChR2)-eYFP fusion protein under a pan-neuronal promoter yielded widespread infection in the GPe. In addition, this gave rise to eYFP-labeled axonal processes terminating throughout the dStr (Fig. 1*b*). The VGAT-immunoreactive puncta on these axons suggest that they have the capacity to release GABA within the dStr (Fig. 1*b*). Because of their dense arborization in the dStr, we hypothesized that they target SPNs, the principal neurons of the dStr. In support of this idea, ultrastructural data suggest that pallidostriatal terminals are juxtaposed to spine-bearing dendrites in the dStr (Mallet et al., 2012). Consistent with our hypothesis, pan-neuronal optogenetic stimulation of the GPe (hereafter called “pan-GPe” input) elicited IPSCs in SPNs (Fig. 1*c*). Consistent with previous observations that GPe neurons target dStr INTs (Bevan et al., 1998; Mallet et al., 2012; Mastro et al., 2014; Hernández et al., 2015; Saunders et al., 2016), optogenetic stimulation of the pan-GPe input evoked IPSCs in dStr INTs, which were identified by their aspiny dendrites (Fig. 1*c*). The biophysical properties of the IPSCs recorded from SPNs and INTs were thus compared. While there was no difference in the synaptic latency, SPNs displayed a larger PPR (SPNs:  $1.41 \pm 0.23$ ,  $n = 92$  cells; INTs:  $0.75 \pm 0.16$ ,  $n = 25$  cells;  $p < 0.0001$ ), longer rise time (SPNs:  $5.9 \pm 1.4$  ms,  $n = 92$  cells; INTs:  $2.6 \pm 1.0$  ms,  $n = 25$  cells;  $p < 0.0001$ ), and longer decay time (SPNs:  $217.0 \pm 44.0$  ms,  $n = 92$  cells; INTs:  $177.0 \pm 41.6$  ms,  $n = 25$  cells;  $p = 0.0277$ ) compared with INTs. These responses were abolished by the application of the GABA<sub>A</sub> receptor antagonist SR95531 (10  $\mu\text{M}$ ; Fig. 1*d*), a finding that is consistent with the GABAergic nature of the GPe (Fahn and Côté, 1968; Jessell et al., 1978; Oertel and Mugnaini, 1984; Oertel et al., 1984).

Parvalbumin-expressing (PV<sup>+</sup>), fast-spiking striatal interneurons (FSIs) are a subclass of INTs that plays a pivotal role in regulating striatal functions (Koós and Tepper, 2002; Tepper and Bolam, 2004; Tepper et al., 2008; Klaus et al., 2011; Gittis and Kreitzer, 2012) and were thus targeted in this analysis. Activation of the pan-GPe input produced IPSCs in all FSIs examined (Fig. 2). While there was no difference in the synaptic latency, SPNs displayed a larger PPR (SPNs:  $1.30 \pm 0.12$ ,  $n = 12$  cells; FSIs:  $0.75 \pm 0.16$ ,  $n = 17$  cells;  $p < 0.0001$ ), longer rise time (SPNs:  $5.2 \pm 0.7$  ms,  $n = 12$  cells; FSIs:  $2.8 \pm 1.1$  ms,  $n = 17$  cells;

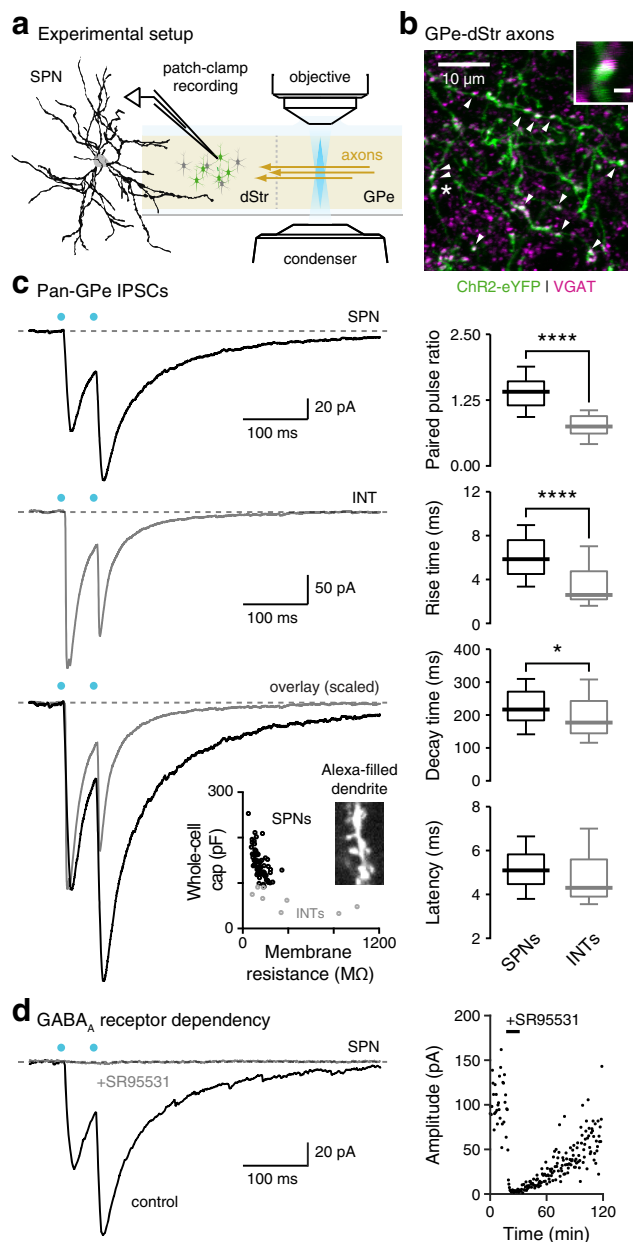


**Figure 1.** Pallidostratial projection targets both spiny projection neurons and interneurons.

**a**, SPNs were identified and patch clamped in *ex vivo* brain slices. An example of a reconstructed SPN is shown. Blue (peak 450 nm) excitation wavelength was delivered locally to the GPe through both the 60× objective and the condenser to trigger GABA release from pallidostratial axons expressing the excitatory opsin ChR2. **b**, Following intrapallidal injection of a constitutive, pan-neuronal hSyn-ChR2-eYFP AAV, ChR2-eYFP-expressing axons (green) and boutons were observed in the dStr under laser-scanning confocal microscopy. The apposition of the vesicular GABA transporter (magenta) is shown as white. An example [marked with an asterisk (“\*\*”) is shown at a higher magnification in the inset. Scale bar, 1  $\mu$ m. **c**, Left, Representative IPSC recordings from an SPN (top, black) and an INT (middle, gray) are shown. A paired-pulse (20 Hz) light stimulation (blue circle) was used to activate the pan-GPe input. Bottom, Traces from the two examples were overlaid and peak-scaled to illustrate the difference in the PPR and kinetics of the IPSCs observed in the two cell classes. Inset, Relationship between whole-cell capacitance and membrane resistance of both SPNs (black) and INTs (gray) is plotted. A photomicrograph is included to illustrate the identification of a typical SPN based on its unique dendritic morphology. Right, Summary data are presented as box plots. SPNs displayed a larger PPR (SPNs:  $1.41 \pm 0.23$ ,  $n = 92$  cells; INTs:  $0.75 \pm 0.16$ ,  $n = 25$  cells;  $p < 0.0001$ , Mann–Whitney *U* test), a longer rise time (SPNs:  $5.9 \pm 1.4$  ms,  $n = 92$  cells; INTs:  $2.6 \pm 1.0$  ms,  $n = 25$  cells;  $p < 0.0001$ , Mann–Whitney *U* test), and a longer decay time (SPNs:  $217.0 \pm 44.0$  ms,  $n = 92$  cells; INTs:  $177.0 \pm 41.6$  ms,  $n = 25$  cells;  $p = 0.0277$ , Mann–Whitney *U* test) relative to INTs. Latency was not different between SPNs and INTs (SPNs:  $4.9 \pm 0.6$  ms,  $n = 12$  cells; INTs:  $4.3 \pm 0.7$  ms,

$p = 0.0015$ ), and longer decay time (SPNs:  $284.0 \pm 35.9$  ms,  $n = 12$  cells; INTs:  $195.7 \pm 46.7$  ms,  $n = 17$  cells;  $p = 0.0051$ ) compared with FSIs from the same animals. However, as FSIs account for only a small fraction of the total striatal INT population, it is very likely that additional subclasses of INTs also receive GPe input, as suggested by earlier studies (Bevan et al., 1998; Saunders et al., 2016).

### GPe input targets both dSPNs and iSPNs

As the balance in the activity of dSPNs and iSPNs in the dStr is crucial for proper motor control (Albin et al., 1989; DeLong, 1990; Kravitz et al., 2010; Freeze et al., 2013; Calabresi et al., 2014; Sippy et al., 2015), it is important to further examine the functional connectivity of the pallidostratial input to both populations of SPNs. To avoid the confounding effects of variable viral infection and inconsistent preservation of pallidostratial axons in the slice preparation on the elicited responses, dSPNs and iSPNs within  $\sim 150 \mu$ m of each other were compared as dSPN–iSPN “pairs” (see Materials and Methods). Identical stimulation sites and light intensities were used for both neurons in each given paired recording. Under these conditions, iSPNs consistently exhibited larger IPSC amplitude compared with those from their dSPN matched pairs (iSPNs,  $94.1 \pm 30.0$  pA; dSPNs =  $52.5 \pm 22.2$  pA;  $n = 12$  pairs;  $p = 0.0122$ ). However, there was no difference in PPR (dSPNs,  $1.58 \pm 0.29$ ; iSPNs =  $1.47 \pm 0.28$ ;  $n = 11$  pairs;  $p > 0.9999$ ), rise time (dSPNs,  $6.8 \pm 1.2$  ms; iSPNs,  $5.1 \pm 1.0$  ms;  $n = 11$  pairs;  $p = 0.0537$ ), or decay time (dSPNs,  $253.4 \pm 38.2$  ms; iSPNs,  $210.6 \pm 8.5$  ms;  $n = 11$  pairs;  $p = 0.2061$ ) between dSPNs and iSPNs. Notably, the GPe–SPN IPSC population data are consistent with all of these findings (Table 2).

### Npas1<sup>+</sup> neurons constitute the primary GPe input to SPNs

The predominant projection from the GPe to the dStr has been proposed to originate primarily from PV<sup>+</sup> neurons (Kita and Kita, 2001; Hoover and Marshall, 2002; Mallet et al., 2012; Mastro et al., 2014). However, discordant results have been observed (Kita et al., 1999). As neurons that form the pallidostratial projection are likely target cell specific (Bevan et al., 1998), we used a monosynaptic rabies virus-tracing method (Ugolini, 2011; Callaway and Luo, 2015; Ghanem and Conzelmann, 2016) to examine the identity of the GPe neurons that synapse onto SPNs.

To target dSPNs and iSPNs, *Drd1a-Cre* and *Drd2-Cre* mice were used, respectively (Fig. 3a). Consistent with previous studies that used rabies viruses to map cortical inputs to SPNs (Wall et al., 2013; Deng et al., 2015; Guo et al., 2015; Kim et al., 2015; Reardon et al., 2016), widespread, retrogradely labeled neurons were evident in the cortex (Fig. 3b). In addition, retrograde labeling of GPe neurons was also evident (Fig. 3b), thus corroborating the electrophysiological analysis demonstrating that connections between GPe neurons and SPNs were monosynaptic. Furthermore, immunohistochemical staining for PV revealed that only a small fraction of these retrogradely labeled GPe neurons were PV<sup>+</sup> ( $0.0 \pm 0.0\%$ ,  $n = 164$  cells). This is statistically different

$n = 17$  cells;  $p = 0.2677$ , Mann–Whitney *U* test). SPN subtypes were not differentiated. **d**, Left, Current records showing the effect of SR95531 on GPe–SPN IPSCs in a representative SPN. Right, A plot of the time course showing the sensitivity of GPe–SPN IPSCs to the application of SR95531 (horizontal bar). Medians  $\pm$  median absolute deviations and two-tailed *p* values are listed. Medians, interquartile ranges, and 10–90th percentiles are also presented in a graphic format. Asterisks denote statistical significance level (\* $p < 0.05$ , \*\*\*\* $p < 0.0001$ , Mann–Whitney *U* test and Wilcoxon signed rank test).

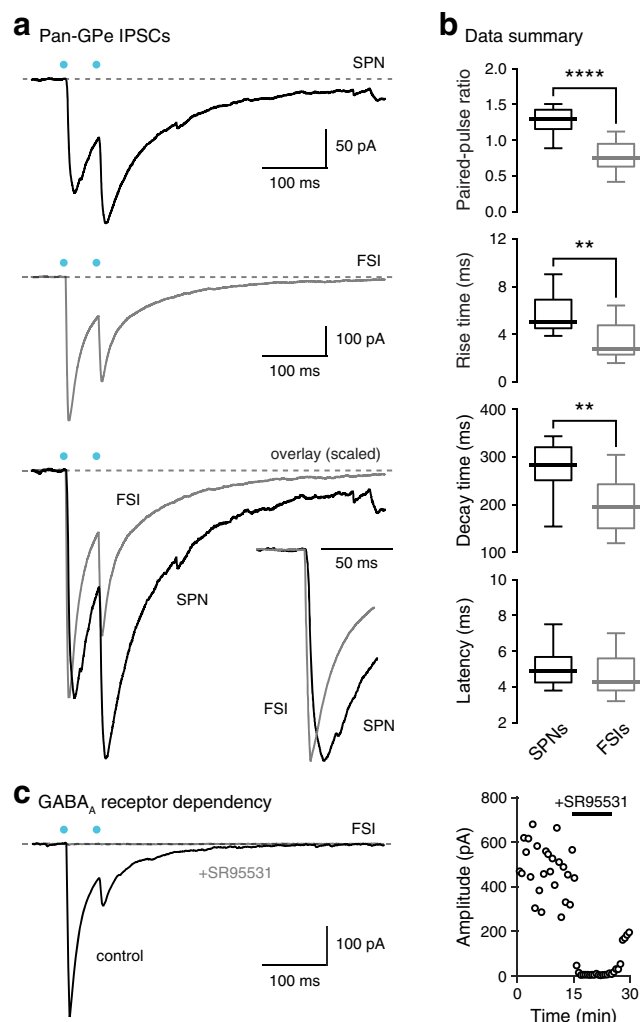


**Figure 2.** Pallidostriatal projection targets fast-spiking interneurons. **a**, Left, Representative IPSC recordings from an SPN (top, black) and an FSI (middle, gray) were shown. A paired-pulse (20 Hz) light stimulation (blue circle) was used to activate the pan-GPe input. Bottom, Traces from the two examples were overlaid and peak-scaled to illustrate the difference in the PPR and kinetics of the IPSCs observed in the two cell classes. Inset, A blown-up version of the first IPSCs. **b**, Summary data are presented as box plots. SPNs displayed a larger PPR (SPNs:  $1.30 \pm 0.12$ ,  $n = 12$  cells; FSIs:  $0.75 \pm 0.16$ ,  $n = 17$  cells;  $p < 0.0001$ , Mann-Whitney  $U$  test), a longer rise time (SPNs:  $5.2 \pm 0.7$  ms,  $n = 12$  cells; FSIs:  $2.8 \pm 1.1$  ms,  $n = 17$  cells;  $p = 0.0015$ , Mann-Whitney  $U$  test), and a longer decay time (SPNs:  $284.0 \pm 35.9$  ms,  $n = 12$  cells; FSIs:  $195.7 \pm 46.7$  ms,  $n = 17$  cells;  $p = 0.0051$ , Mann-Whitney  $U$  test) relative to FSIs. Latency was not different between SPNs and FSIs (SPNs:  $4.9 \pm 0.6$  ms,  $n = 12$  cells; FSIs:  $4.3 \pm 0.7$  ms,  $n = 17$  cells;  $p = 0.2677$ , Mann-Whitney  $U$  test). For this dataset, SPNs and FSIs were both from the PV reporter (*Pvalb-Cre;R26<sup>LSL</sup>-tdTomato*) line; accordingly, SPN subtypes were not differentiated. Medians  $\pm$  median absolute deviations and two-tailed  $p$  values are listed. **c**, Left, Current records showing the effect of SR95531 on GPe-FSI IPSCs in a representative FSI. Right, A plot of the time course showing the sensitivity of GPe-FSI IPSCs to the application of SR95531 (horizontal bar). Medians, interquartile ranges, and 10–90th percentiles are also presented in a graphic format. Asterisks denote statistical significance level (\*\* $p < 0.01$ , \*\*\*\* $p < 0.0001$ , Mann-Whitney  $U$  test and Wilcoxon signed rank test).

from the abundance of PV<sup>+</sup> neurons in the total GPe population ( $55.3 \pm 6.2\%$ ,  $n = 1792$  cells,  $p < 0.0001$ ). As the expression patterns of PV and the transcription factor Npas1 in the GPe are segregated (Flandin et al., 2010; Nóbrega-Pereira et al., 2010; Abdi et al., 2015; Hernández et al., 2015), we hypothesize that these SPN-targeting, PV<sup>−</sup> GPe neurons are largely Npas1<sup>+</sup>.

To this end, we used *Pvalb-Cre* (Hippenmeyer et al., 2005) and *Npas1-Cre* (Hernández et al., 2015) transgenic lines to further

**Table 2.** GPe-SPN IPSC properties in naïve mice

	<i>p</i> value*	Median	Median absolute deviation	Sample size	
				Cells	Mice
<b>Pan-GPe input</b>					
Amplitude (pA)					
dSPNs	<b>0.0220</b>	56.9	19.1	35	25
iSPNs		89.5	41.4	47	33
PPR					
dSPNs	0.8063	1.47	0.19	33	25
iSPNs		1.41	0.25	47	33
Rise time (ms)					
dSPNs	0.7949	6.2	1.4	33	25
iSPNs		5.9	1.8	47	33
Decay time (ms)					
dSPNs	0.1387	231.3	45.0	33	25
iSPNs		202.7	33.3	47	33
Latency (ms)					
dSPNs	0.4789	5.1	0.5	33	25
iSPNs		5.1	0.8	47	33
<b>Npas1<sup>+</sup> input</b>					
Amplitude (pA)					
dSPNs	<b>0.0002</b>	64.5	21.6	27	9
iSPNs		138.2	50.9	29	9
PPR					
dSPNs	0.7938	1.22	0.21	25	9
iSPNs		1.29	0.17	28	9
Rise time (ms)					
dSPNs	0.8981	6.1	1.3	25	9
iSPNs		6.3	2.1	28	9
Decay time (ms)					
dSPNs	0.8487	269.8	49.1	25	9
iSPNs		247.5	28.2	28	9
Latency (ms)					
dSPNs	0.6611	5.0	0.4	25	9
iSPNs		5.0	0.5	28	9

\*Mann-Whitney test; two-tailed exact  $p$  values are shown.  $p$  values  $< 0.05$  are shown in bold.

assess the contribution of these two populations of GPe neurons to the pallidostriatal projection to SPNs. A CreOn Chr2-eYFP-expressing AAV was used to visualize the Npas1<sup>+</sup> and PV<sup>+</sup> GPe input to the dStr in *Npas1-Cre* and *Pvalb-Cre* mice, respectively. As illustrated in Figure 3c, Npas1<sup>+</sup> GPe neurons exhibited widespread and dense axonal arborization within the dStr. On the other hand, the density of eYFP-labeled PV<sup>+</sup> GPe axons was much lower (Npas1<sup>+</sup> =  $18.6 \pm 5.7$  a.u.,  $n = 9$  ROIs; PV<sup>+</sup> =  $4.3 \pm 1.2$  a.u.,  $n = 9$  ROIs;  $p < 0.0001$ ; Fig. 3d). As our ability to selectively express Chr2-eYFP in distinct GPe cell types (Npas1<sup>+</sup> neurons vs PV<sup>+</sup> neurons) is crucial to our analysis, we assessed the presence of photocurrent in genetically identified Npas1<sup>+</sup> neurons and PV<sup>+</sup> GPe neurons. Npas1<sup>+</sup> GPe neurons in *Npas1-Cre* mice expressed photocurrent at the same percentage, as did PV<sup>+</sup> GPe neurons in *Pvalb-Cre* mice (*Npas1-Cre* = 91.7%,  $n = 12$  cells; *Pvalb-Cre* = 88.9%,  $n = 36$  cells;  $p = 1.0000$ ); photocurrent was observed in none of the non-Cre-expressing GPe neurons (*Npas1-Cre* = 0 of 21 cells; *Pvalb-Cre* = 0 of 44 cells). Optogenetic stimulation of the PV<sup>+</sup> GPe input yielded a smaller IPSC amplitude relative to the Npas1<sup>+</sup> GPe input in both dSPNs (PV<sup>+</sup> input:  $0 \pm 0$  pA,  $n = 23$  cells; Npas1<sup>+</sup> input:  $64.5 \pm 21.6$  pA,  $n = 27$  cells;  $p < 0.0001$ ) and iSPNs (PV<sup>+</sup> input:  $0 \pm 0$  pA,  $n = 13$  cells; Npas1<sup>+</sup> input:  $138.2 \pm 50.9$  pA,  $n = 29$  cells;  $p < 0.0001$ ; Fig. 3e). This is consistent with the observations that GPe PV<sup>+</sup> neurons target primarily FSIs and other INTs, but not SPNs, in the dStr (Bevan et al., 1998; Mastro et al., 2014). As only a small subset of SPNs sampled received the PV<sup>+</sup> GPe input (see below), the median IPSC amplitude is zero.



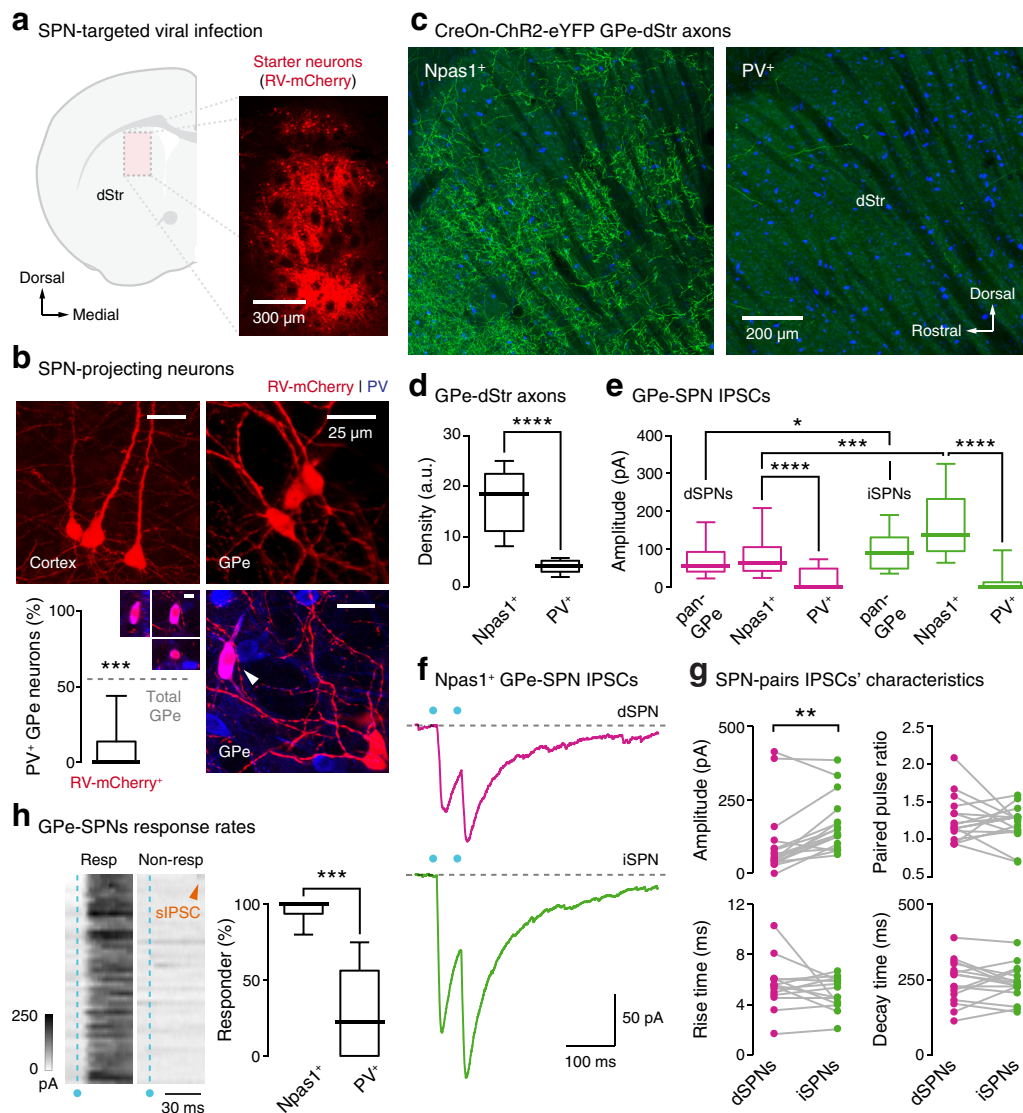


**Figure 3.** *Npas1*<sup>+</sup> GPe neurons constitute the primary pallidal input to the dStr. **a**, Left, a schematic diagram of a coronal mouse brain section illustrating the location of the virus injections for monosynaptic tracing. *Drd1a-Cre* and *Drd2-Cre* were used to target dSPNs and iSPNs, respectively. Right, A photomicrograph showing the center of infection and mCherry-expressing, rabies virus-infected (RV-mCherry<sup>+</sup>) SPNs. **b**, Top left, As a proof-of-concept, retrogradely labeled layer 5 cortical neurons are shown. Top right, Representative retrogradely labeled neurons (red) in the GPe. Bottom right, Immunohistochemistry for PV is shown in blue. An example of a PV<sup>+</sup> retrogradely labeled neuron is shown (magenta, arrowhead). Orthogonal projections of this neuron are shown as an inset (bottom left). Scale bar, 10  $\mu$ m. Two PV<sup>−</sup> retrogradely labeled neurons (red) are clearly visible at the lower right corner of the field. Bottom left, A box plot summarizing the abundance of PV<sup>+</sup> GPe neurons retrogradely labeled with RV-mCherry<sup>+</sup>. This is less than the total number of PV<sup>+</sup> neurons in the GPe as a whole (RV-mCherry<sup>+</sup>:  $0.0 \pm 0.0\%$ ,  $n = 21$  sections; total:  $55.3 \pm 6.2\%$ ,  $n = 15$  sections;  $p < 0.0001$ , Mann–Whitney  $U$  test). Data from both *Drd1a-Cre* (4 of 75 cells, 5.3%) and *Drd2-Cre* (7 of 89 cells, 7.9%) are not different ( $p = 0.8630$ ) and are thus pooled. **c**, Sagittal brain sections showing the density of ChR2-eYFP-labeled GPe axons in the rostradorsal area of the dStr in an *Npas1-Cre* mouse (left) and a *Pvalb-Cre* mouse (right). Sections were also immunolabeled for HuCD (blue) to decipher the cytoarchitecture. Note, the top left dark area corresponds to the external capsule. A single confocal optical section is illustrated in both examples. Scale bar applies to both panels in **c**. **d**, *Npas1*<sup>+</sup>:  $18.6 \pm 5.7$  a.u.,  $n = 9$  ROIs; *PV*<sup>+</sup>:  $4.3 \pm 1.2$  a.u.,  $n = 9$  ROIs,  $p < 0.0001$ , Mann–Whitney  $U$  test. **e**, Response amplitudes of the pan-, *Npas1*<sup>+</sup>, and *PV*<sup>+</sup> GPe input to dSPNs (magenta) and iSPNs (green) are summarized in box plots. IPSC amplitude from the *PV*<sup>+</sup> GPe input was smaller relative to the *Npas1*<sup>+</sup> GPe input in both dSPNs (*PV*<sup>+</sup> input:  $0 \pm 0$  pA,  $n = 23$  cells; *Npas1*<sup>+</sup> input:  $64.5 \pm 21.6$  pA,  $n = 27$  cells;  $p < 0.0001$ , Mann–Whitney  $U$  test) and iSPNs (*PV*<sup>+</sup> input:  $0 \pm 0$  pA,  $n = 13$  cells; *Npas1*<sup>+</sup> input:  $138.2 \pm 50.9$  pA,  $n = 29$  cells;  $p < 0.0001$ , Mann–Whitney  $U$  test). IPSC amplitude was larger in iSPNs compared with dSPNs from both pan-GPe input (iSPNs:  $89.5 \pm 41.4$  pA,  $n = 47$  cells; dSPNs:  $56.9 \pm 19.1$  pA,  $n = 35$  cells;  $p = 0.0220$ , Mann–Whitney  $U$  test) and *Npas1*<sup>+</sup> GPe input (dSPNs:  $64.5 \pm 21.6$  pA,  $n = 27$  cells; iSPNs:  $138.2 \pm 50.9$  pA,  $n = 29$  cells;  $p = 0.0002$ , Mann–Whitney  $U$  test). **f**, Representative recordings of *Npas1*<sup>+</sup> GPe-dSPN (top, magenta) and GPe-iSPN IPSCs (bottom, green). **g**, Box plots summarizing the properties of *Npas1*<sup>+</sup> GPe IPSCs in dSPN–iSPN pairs. iSPNs exhibited larger amplitude (top left; iSPNs,  $134.1 \pm 40.3$  pA; dSPNs =  $55.3 \pm 23.5$  pA;  $n = 17$  pairs;  $p = 0.0017$ , Wilcoxon signed rank test) relative to dSPNs. However, there was no difference in PPR (top right; dSPNs,  $1.18 \pm 0.17$ ; iSPNs,  $1.26 \pm 0.13$ ;  $n = 16$  pairs;  $p = 0.6322$ , Wilcoxon signed rank test), rise time (bottom left; dSPNs,  $5.6 \pm 0.7$  ms; iSPNs,  $5.6 \pm 1.1$  ms;  $n = 16$  pairs;  $p = 0.2030$ , Wilcoxon signed rank test), or decay time (bottom right; dSPNs,  $247.0 \pm 50.1$  ms; iSPNs,  $234.1 \pm 28.0$  ms;  $n = 16$  pairs;  $p = 0.5966$ , Wilcoxon signed rank test). **h**, Left, Grayscale representation of GPe-SPN IPSCs in a “responder” neuron. Each row represents a single trial. Blue circles and dotted lines indicate the timing of the optogenetic stimulation of the GPe. A “nonresponder” neuron (right) is included for comparison. A spontaneous IPSC is highlighted (orange arrow). Right, Response rate of SPNs to different GPe inputs (*Npas1*<sup>+</sup> input:  $100.0 \pm 0\%$ ,  $n = 9$  mice; *PV*<sup>+</sup> input:  $22.5 \pm 22.5\%$ ,  $n = 6$  mice;  $p = 0.0002$ ). For simplicity, dSPNs (*Npas1*<sup>+</sup> input, 27 cells; *PV*<sup>+</sup> input, 22 cells) and iSPNs (*Npas1*<sup>+</sup> input, 29 cells; *PV*<sup>+</sup> input, 13 cells) are pooled. Medians  $\pm$  median absolute deviations and two-tailed  $p$  values are listed. Medians, interquartile ranges, and 10–90th percentiles are also presented in a graphic format. Asterisks denote statistical significance level (\* $p < 0.05$ , \*\* $p < 0.01$ , \*\*\* $p < 0.001$ , \*\*\*\* $p < 0.0001$ , Mann–Whitney  $U$  test and Wilcoxon signed rank test).

Given that  $Npas1^{+}$  GPe neurons appeared to constitute the main pallidostriatal input to SPNs, we further analyzed the  $Npas1^{+}$  GPe input to dSPN–iSPN pairs. Stimulation of  $Npas1^{+}$  GPe neurons yielded IPSCs in iSPNs with larger amplitude (iSPNs,  $134.1 \pm 40.3$  pA; dSPNs,  $55.3 \pm 23.5$  pA;  $n = 17$  pairs;  $p = 0.0017$ ) relative to IPSCs in dSPNs. In contrast, there was no difference in PPR (dSPNs,  $1.18 \pm 0.17$ ; iSPNs,  $1.26 \pm 0.13$ ;  $n = 16$  pairs;  $p = 0.6322$ ), rise time (dSPNs,  $5.6 \pm 0.7$  ms; iSPNs,  $5.6 \pm 1.1$  ms;  $n = 16$  pairs;  $p = 0.2030$ ), and decay time (dSPNs,  $247.0 \pm 50.1$  ms; iSPNs,  $234.1 \pm 28.0$  ms;  $n = 16$  pairs;  $p = 0.5966$ ; Fig. 3*fg*). These findings largely recapitulated the differences seen with the pan-GPe input (Table 2), further demonstrating that the GPe input to SPNs arises primarily from  $Npas1^{+}$  GPe neurons.

To further delineate the relative contribution of  $Npas1^{+}$  GPe neurons to the total pallidostriatal input to SPNs, a comparative analysis of the response rate of SPNs to different GPe inputs was performed. At the population level, >90% of all recorded SPNs (dSPNs: 92.6%,  $n = 27$  cells; iSPNs: 96.6%,  $n = 29$  cells) received input from  $Npas1^{+}$  GPe neurons. In contrast, a much smaller fraction of recorded SPNs receives input from  $PV^{+}$  GPe neurons (dSPNs: 39.1%,  $n = 23$  cells; iSPNs: 23.1%,  $n = 13$  cells;  $p < 0.0001$ ). As multiple SPNs ( $n = 6 \pm 2$  cells) were typically sampled from each mouse, the response rate of SPNs to GPe input was computed for each mouse. In agreement with the population data, the response rate of SPNs to  $Npas1^{+}$  GPe input across mice was consistently high (dSPNs:  $100 \pm 0\%$ ,  $n = 9$  mice; iSPNs:  $100 \pm 0\%$ ,  $n = 9$  mice) and greater ( $p = 0.0002$ ) than the response rate of SPNs to  $PV^{+}$  GPe input (dSPNs:  $0 \pm 33.4\%$ ,  $n = 6$  mice; iSPNs:  $0 \pm 0\%$ ,  $n = 5$  mice; Fig. 3*h*). To confirm that the relatively low response rate with viral-mediated optogenetic stimulation of  $PV^{+}$  GPe neurons was not a result of unreliable ChR2 expression, additional experiments were performed with a mouse line carrying a floxed-stop ChR2-eYFP allele driven by the *Pvalb* promoter. Experiments with this mouse line yielded results similar to those derived using the viral approach (9.1%,  $n = 11$  cells,  $p = 0.1467$ ). Last, as the GPe contains cholinergic GPe neurons (Gritti et al., 2006; Nóbrega-Pereira et al., 2010; Abdi et al., 2015; Hernández et al., 2015) that have the potential to corelease GABA (Tkatch et al., 1998; Saunders et al., 2015), their input to SPNs was examined with the *ChAT-Cre* and floxed-stop ChR2-eYFP mice. However, direct GABAergic input to SPNs from cholinergic GPe neurons was not detected (0%,  $n = 7$  cells). Altogether, optogenetics-based mapping experiments corroborate the rabies-tracing findings that  $Npas1^{+}$  GPe neurons constitute the primary pallidostriatal projection to both dSPNs and iSPNs. To demonstrate that the connection between  $Npas1^{+}$  GPe neurons and SPNs is monosynaptic, GABA transmission was monitored under conditions in which action potential propagation was blocked (with  $1 \mu\text{M}$  tetrodotoxin and  $100 \mu\text{M}$  4-aminopyridine; Petreanu et al., 2009). Terminal field stimulation of the  $Npas1^{+}$  GPe input successfully evoked IPSCs in nine of nine SPNs, thus confirming the monosynaptic nature of this connection.

We have previously observed a low density of axonal projections from the  $Npas1^{+}$  GPe neurons to the STN (Hernández et al., 2015). To further investigate the differences in the projection characteristics of  $Npas1^{+}$  GPe neurons and  $PV^{+}$  GPe neurons, we examined the spatial relationship between VGAT and GPe–STN axons. As illustrated in Figure 4*a*, VGAT-immunoreactive puncta were associated with  $PV^{+}$  GPe–STN axons and  $Npas1^{+}$  GPe–STN axons. To assess the strength and prevalence of the

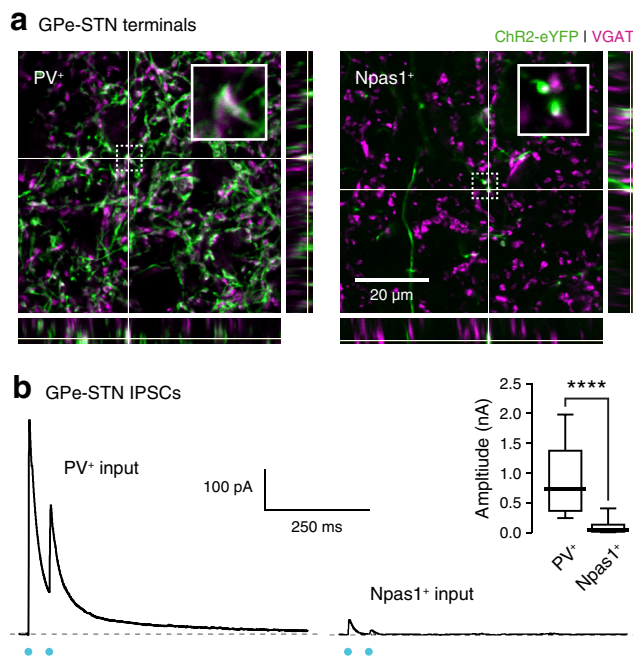


**Figure 4.**  $PV^{+}$  GPe neurons constitute the primary pallidal input to the STN. *a*, High-magnification images showing the spatial relationship between vesicular GABA transporter terminals (magenta) with axons (green) from  $PV^{+}$  neurons (left) and  $Npas1^{+}$  neurons (right). Rectangular images showing orthogonal projections. Crosshairs indicate the projected planes. Insets show high-magnification views of areas within the squares (dotted line). Scale bar applies to both panels in *a*. *b*, Sample current traces showing the responsiveness of STN neurons to paired-pulse (20 Hz) optogenetic activation (blue) of  $PV^{+}$  GPe input (left) and  $Npas1^{+}$  GPe input (right;  $PV^{+} = 738.0 \pm 409.0$  pA,  $n = 18$  cells;  $Npas1^{+} = 40.3 \pm 19.1$  pA,  $n = 16$  cells;  $p < 0.0001$ , Mann–Whitney *U* test). Medians  $\pm$  median absolute deviations and two-tailed *p* values are listed. Medians, interquartile ranges, and 10–90th percentiles are also presented in a graphic format (\*\*\*\* $p < 0.0001$ , Mann–Whitney *U* test).

connectivity of these axons with STN neurons, whole-cell voltage-clamp recordings were performed in STN neurons. Terminal field optogenetic activation of  $PV^{+}$  GPe input reliably evoked large IPSCs with a low-chloride internal solution in 17 of 18 STN neurons (94%) examined, while 11 of 16 STN neurons (~70%) responded to  $Npas1^{+}$  GPe input, with IPSCs that were over an order of magnitude smaller ( $PV^{+}$  input:  $738.0 \pm 409.0$  pA,  $n = 18$  cells;  $Npas1^{+}$  input:  $40.3 \pm 19.1$  pA,  $n = 16$  cells;  $p < 0.0001$ ; Fig. 4*b*). These findings are consistent with those in previous studies indicating that  $PV^{+}$  GPe neurons constitute the principal GPe projection to the STN (Hoover and Marshall, 1999, 2002; Mastro et al., 2014; Abdi et al., 2015; Hernández et al., 2015).

### GPe–SPN input is enhanced following chronic 6-OHDA lesion

Compelling evidence suggests that pathological activity in the GPe contributes to motor symptoms in PD (Zaragoza et al., 1992; Hauber et al., 1998; Rajput et al., 2008; Johnson et al., 2012; Vitek et al., 2012; Abedi et al., 2013). In PD animal models, GPe neurons exhibit reduced firing rates *ex vivo* and *in vivo* (Filion and Tremblay, 1991; Mallet et al., 2008; Chan et al., 2011; Lemaire et al., 2012; Hernández et al., 2015). Since the imbalance in information processing between the direct and indirect dStr projection pathways has been strongly linked to motor symptoms in PD (Albin et al., 1989; DeLong, 1990; Kravitz et al., 2010), it is important to determine the physiological effects of chronic dopa-



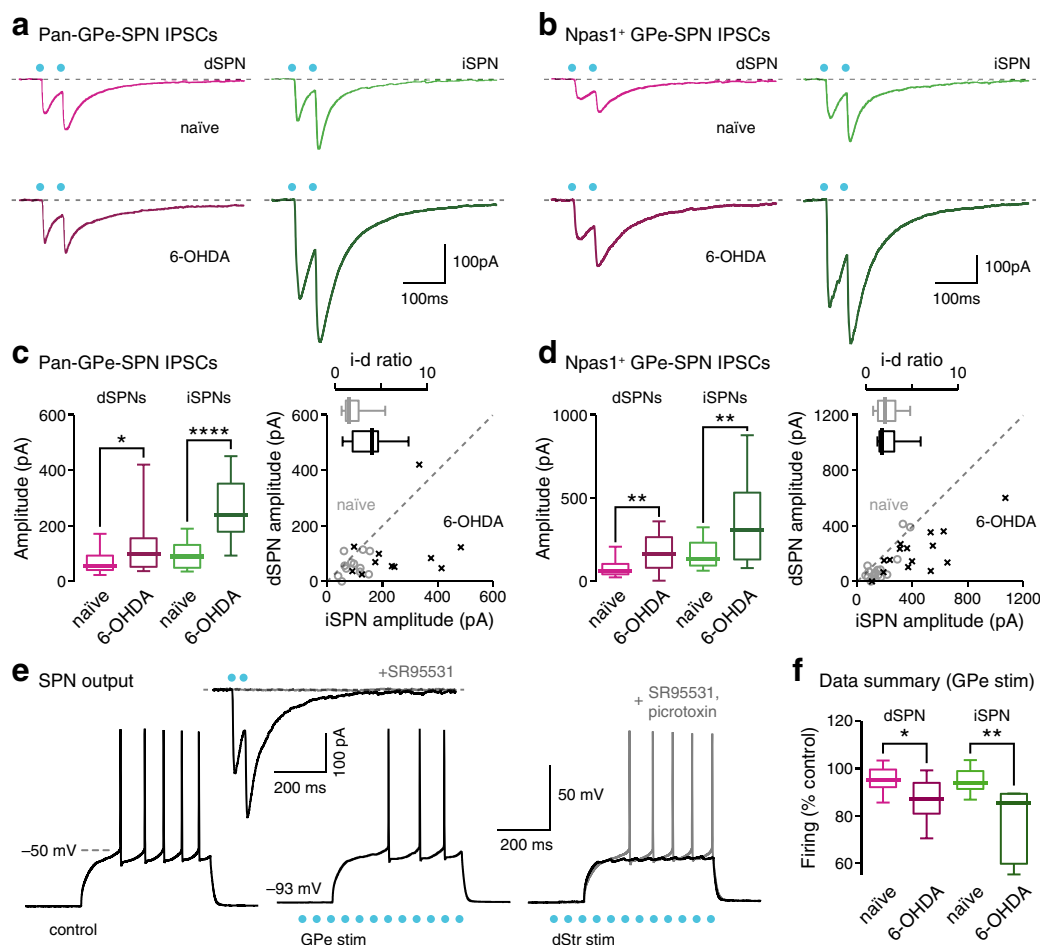


**Figure 5.** GPe-SPN input is enhanced in a mouse model of Parkinson's disease. **a**, Representative pan-GPe-SPN IPSCs from naïve mice (magenta and green) and a chronic 6-OHDA lesioned mouse model of Parkinson's disease (maroon and dark green). **b**, Representative Npas1<sup>+</sup> GPe-SPN IPSCs from naïve mice (magenta and green) and a chronic 6-OHDA lesioned mouse model of Parkinson's disease (maroon and dark green). **c**, Left, Box plots summarizing the amplitude of pan-GPe-SPN population IPSCs from naïve mice (magenta and green) and chronic 6-OHDA lesioned mice (maroon and dark green). An increase in IPSC amplitude was observed in chronic 6-OHDA lesioned mice from both dSPNs (naïve:  $56.9 \pm 19.1$  pA,  $n = 35$  cells; 6-OHDA:  $99.8 \pm 47.2$  pA,  $n = 19$  cells;  $p = 0.0285$ , Mann–Whitney  $U$  test) and iSPNs (naïve:  $89.5 \pm 41.4$  pA,  $n = 47$  cells; 6-OHDA:  $240.4 \pm 98.8$  pA,  $n = 36$  cells;  $p < 0.0001$ , Mann–Whitney  $U$  test) compared with naïve mice. Right, dSPN–iSPN pairs from naïve (gray,  $n = 11$  cells) and chronic 6-OHDA lesioned mice (black,  $n = 12$  cells). Each symbol represents a dSPN–iSPN pair. Inset, The ratio of IPSC amplitude between dSPN–iSPN pairs in naïve mice (gray) and chronic 6-OHDA-lesioned mice (black) was calculated and denoted as “i-d ratio.” There was no difference in the i-d ratios of chronic 6-OHDA lesioned mice (black) and naïve mice (gray;  $p = 0.1007$ ). **d**, Left, Box plots summarizing the amplitude of Npas1<sup>+</sup> GPe-SPN population IPSCs from naïve mice (magenta and green) and chronic 6-OHDA lesioned mice (maroon and dark green). An increase in IPSC amplitude was observed in chronic 6-OHDA lesioned mice from both dSPNs (naïve:  $64.5 \pm 21.6$  pA,  $n = 27$  cells; 6-OHDA:  $164.7 \pm 91.0$  pA,  $n = 20$  cells;  $p = 0.0036$ , Mann–Whitney  $U$  test) and iSPNs (naïve:  $138.2 \pm 50.9$  pA,  $n = 29$  cells; 6-OHDA:  $311.3 \pm 194.2$  pA,  $n = 29$  cells;  $p = 0.0026$ , Mann–Whitney  $U$  test) compared with naïve mice. Right, Comparison of dSPN–iSPN pairs from naïve (gray,  $n = 16$  cells) and chronic 6-OHDA lesioned mice (black,  $n = 14$  cells). Each symbol represents a dSPN–iSPN pair. Inset, The i-d ratio is not different between naïve mice (gray) and 6-OHDA lesioned mice (black;  $p > 0.9999$ ). **e**, Sample voltage traces of an iSPN from a chronic 6-OHDA lesioned mouse. Left, Excitability of SPNs was measured using a single current step that generated five action potentials in the control condition. Middle, GPe stimulation of pallidostriatal axons suppressed iSPN firing. Right, Terminal field stimulation (dStr stim) of pallidostriatal axons abolished iSPN firing (black). Right, This effect was reversed with the coapplication of SR95531 (10  $\mu$ M) and picrotoxin (100  $\mu$ M; gray). Inset, A representative Npas1<sup>+</sup> GPe-iSPN IPSCs from a chronic 6-OHDA lesioned mouse showing the sensitivity of the GPe input to a GABA<sub>A</sub> receptor antagonist, SR95531. **f**, Box plots summarizing the impact of the pan-GPe input stimulation on SPN excitability in naïve and chronic 6-OHDA lesioned mice. 6-OHDA iSPNs exhibited a reduction in the relative firing rate compared with the effect seen in naïve iSPNs (naïve:  $94.0 \pm 3.1\%$ ,  $n = 10$  cells; 6-OHDA:  $85.5 \pm 3.8\%$ ,  $n = 6$  cells;  $p = 0.0017$ , Mann–Whitney  $U$  test). Similarly, 6-OHDA dSPNs also exhibited a reduction in the relative firing compared with the response in naïve dSPNs (naïve:  $95.1 \pm 3.6\%$ ,  $n = 10$  cells; 6-OHDA:  $87.1 \pm 3.8\%$ ,  $n = 6$  cells;  $p = 0.0415$ , Mann–Whitney  $U$  test). Medians  $\pm$  median absolute deviations and two-tailed  $p$  values are listed. Medians, interquartile ranges, and 10–90th percentiles are also presented in a graphic format. Asterisks denote statistical significance level (\* $p < 0.05$ , \*\* $p < 0.01$ , \*\*\* $p < 0.0001$ , Mann–Whitney  $U$  test and Wilcoxon signed rank test).

mine depletion on pallidostriatal signaling in SPNs. In this study, we used unilateral stereotaxic lesions of the nigrostriatal pathway using the injection of the neurotoxin 6-OHDA. 6-OHDA-injected mice that exhibited sensorimotor behavioral deficits associated with a near-complete chronic unilateral lesion of the nigrostriatal pathway (Chan et al., 2011, 2012; Glajch et al., 2012) were used to assess the physiological properties of the pallidostriatal input.

An increase in the IPSC amplitude of the pan-GPe input to dSPNs (naïve:  $56.9 \pm 19.1$  pA,  $n = 35$  cells; 6-OHDA:  $99.8 \pm 47.2$

pA,  $n = 19$  cells;  $p = 0.0285$ ) and iSPNs (naïve:  $89.5 \pm 41.4$  pA,  $n = 47$  cells; 6-OHDA:  $240.4 \pm 98.8$  pA,  $n = 36$  cells;  $p < 0.0001$ ) was observed following chronic 6-OHDA lesion (Fig. 5a,c). Similarly, there was an increase in IPSC amplitude of the Npas1<sup>+</sup> GPe input to both dSPNs (naïve:  $64.5 \pm 21.6$  pA,  $n = 27$  cells; 6-OHDA:  $164.7 \pm 91.0$  pA,  $n = 20$  cells;  $p = 0.0036$ ) and iSPNs (naïve:  $138.2 \pm 50.9$  pA,  $n = 29$  cells; 6-OHDA:  $311.3 \pm 194.2$  pA,  $n = 29$  cells;  $p = 0.0026$ ) in chronic 6-OHDA lesioned mice (Fig. 5b,d). The IPSC amplitude of the PV<sup>+</sup> GPe input to iSPNs increased (naïve:  $0 \pm 0$  pA,  $n = 13$  cells; 6-OHDA:  $46.8 \pm 46.8$  pA,

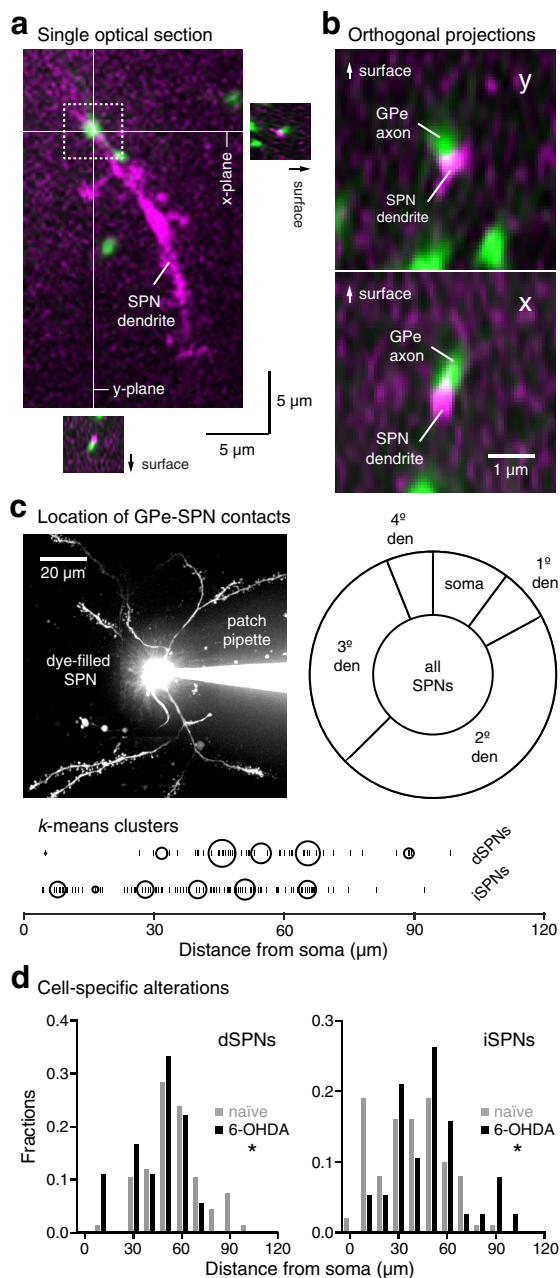


**Figure 6.** GPe input targets dendrites of dSPNs and iSPNs. **a**, Top left, A single optical section showing a representative contact formed between an eYFP<sup>+</sup> GPe axon (green) and an SPN dendrite (magenta) in an *ex vivo* slice. Square images show orthogonal *x*-projection (bottom) and *y*-projection (right). Crosshairs indicate the projected planes. **b**, Enlarged and rotated view of the *x*-projections (bottom) and *y*-projections (top) of the GPe-SPN contact shown in **a**. **c**, Top left, A composite micrograph of the somatodendritic morphology of an Alexa Fluor-filled SPN in an *ex vivo* slice. The branch order of dendrites can be easily discerned. Top right, Graphic representation of the subcellular compartments of SPNs contacting with eYFP<sup>+</sup> GPe axons in naive mice ( $n = 174$  contacts). The majority of the contacts occur on dendrites of both dSPNs ( $n = 67$  contacts) and iSPNs ( $n = 107$  contacts). Approximately 90% of all GPe-SPN contacts were formed on the secondary (dSPNs = 46.3%,  $n = 31$  contacts; iSPNs = 43.9%,  $n = 47$  contacts), tertiary (dSPNs: 38.8%,  $n = 26$  contacts; iSPNs: 23.4%,  $n = 25$  contacts), and quaternary (dSPNs: 7.5%,  $n = 5$  contacts; iSPNs: 4.7%,  $n = 5$  contacts) dendrites. Contacts on somatic regions (dSPNs: 1.5%,  $n = 1$  contact; iSPNs: 18.7%,  $n = 20$  contacts) and primary dendrites (dSPNs: 4.5%,  $n = 3$  contacts; iSPNs: 9.3%,  $n = 10$  contacts) of SPNs were scarce. The relative distribution of GPe-SPN contacts in different subcellular compartments differs between dSPNs and iSPNs ( $p = 0.0039$ , Fisher's exact test). Bottom, A graphic representation showing the distribution of GPe-SPN contacts in naive mice. The size of the *k*-means cluster (circles) denotes the relative density of contacts (vertical lines). **d**, Histogram showing the Euclidean distances of GPe-SPN contacts as a function of eccentricity. A difference in GPe-dSPN contact location (left)

$n = 20$  cells;  $p = 0.0367$ ) following chronic 6-OHDA lesion, but there was no alteration of the PV<sup>+</sup> GPe input to dSPNs (naive:  $0 \pm 0$  pA,  $n = 23$  cells; 6-OHDA:  $37.6 \pm 37.6$  pA,  $n = 11$  cells;  $p = 0.2282$ ). When neighboring dSPNs and iSPNs were compared as matched pairs, we found that chronic 6-OHDA lesion did not alter the relative strength of the GPe input to iSPNs and dSPNs, as represented by the ratio of the IPSC amplitudes of iSPNs to those of dSPNs (i-d ratio; pan-GPe<sub>naive</sub>:  $1.53 \pm 0.39$ ,  $n = 11$  pairs; pan-GPe<sub>6-OHDA</sub>:  $3.94 \pm 1.42$ ,  $n = 11$  pairs;  $p = 0.1007$ ; Npas1<sup>+</sup> input<sub>naive</sub>:  $2.04 \pm 0.89$ ,  $n = 16$  pairs; Npas1<sup>+</sup> input<sub>6-OHDA</sub>:  $1.76 \pm 0.44$ ,  $n = 14$  pairs;  $p > 0.9999$ ). Additionally, using the proportion of responder neurons as a metric, no alteration in the gross connectivity pattern to SPNs before and after chronic 6-OHDA lesion was observed for Npas1<sup>+</sup> GPe input (naive: 94.6%,  $n = 56$  cells; 6-OHDA: 93.9%,  $n = 49$  cells;  $p = 1.0000$ ). However, more SPNs responded to PV<sup>+</sup> GPe input after chronic 6-OHDA lesion (naive: 29.4%,  $n = 34$  cells; 6-OHDA: 58.1%,  $n = 31$  cells;  $p = 0.0255$ ). Furthermore, IPSC amplitude from the pan-GPe input to PV<sup>+</sup> FSIs also was not altered following chronic 6-OHDA lesion (naive:  $600.7 \pm 491.5$  pA,  $n = 17$  cells; 6-OHDA:  $868.7 \pm 530.1$  pA,  $n = 31$  cells;  $p = 0.1054$ ).

### GPe input dampens SPN output in chronic 6-OHDA lesioned mice

Our data firmly established a connection between the GPe and SPNs. However, the functional role of this inhibitory pathway has not been illustrated. The prevailing circuit model predicts that the loss of dopaminergic input to the basal ganglia in PD creates an imbalance in the output of SPNs (Albin et al., 1989). Because of the GABAergic nature of the GPe-SPN input, strengthening of this connection should dampen the output of SPNs.

To assay the functional impact of the GPe-SPN input, we measured its effect on SPN firing driven by current injection. Because the severing of axons is a common problem with all *ex vivo* slice preparations, we stimulated the terminal field of the pallidostriatal axons to recruit the maximum number of synapses distributed across the entire somatodendritic axis of the recorded SPNs (Gertler et al., 2008). In keeping with the GABAergic nature of the GPe-SPN input, its activation suppressed firing in SPNs. This action was abolished upon the application of GABA<sub>A</sub> receptor antagonists (SR95531 and picrotoxin; Fig. 5e). To avoid the confounding effects associated with unintentional activation of local striatal neurons, only the GPe was stimulated in subsequent experiments. We found that dSPNs and iSPNs from both naive and chronic 6-OHDA lesioned mice exhibited a decrease in firing in response to the pan-GPe input (Fig. 5e,f). Importantly, iSPNs from chronic 6-OHDA lesioned mice exhibited a larger reduction in firing compared with the effect seen in naive iSPNs (naive:  $94.0 \pm 3.1\%$ ,  $n = 10$  cells; 6-OHDA:  $85.5 \pm 3.8\%$ ,  $n = 6$  cells;  $p = 0.0017$ ; Fig. 5e,f). Similarly, 6-OHDA dSPNs also yielded a larger reduction in firing compared with the response in naive dSPNs (naive:  $95.1 \pm 3.6\%$ ,  $n = 10$  cells; 6-OHDA:  $87.1 \pm 3.8\%$ ,  $n = 6$  cells;  $p = 0.0415$ ).

←

between naive (black) and chronic 6-OHDA lesioned (gray) mice is observed (naive:  $52.0 \pm 10.4$   $\mu$ m,  $n = 67$  contacts; 6-OHDA:  $48.4 \pm 9.2$   $\mu$ m,  $n = 18$  contacts;  $p = 0.0363$ , Mann-Whitney *U* test). Similarly, a difference in GPe-iSPN contact location (right) between naive (black) and chronic 6-OHDA lesioned (gray) mice is observed (naive:  $39.9 \pm 15.0$   $\mu$ m,  $n = 107$  contacts; 6-OHDA:  $49.3 \pm 14.7$   $\mu$ m,  $n = 38$  contacts;  $p = 0.0367$ , Mann-Whitney *U* test). Medians  $\pm$  median absolute deviations and two-tailed *p* values are listed (\* $p < 0.05$ , Mann-Whitney *U* test).

### GPe inputs to dSPNs and iSPNs are enhanced via distinct mechanisms

What could explain the enhancement of the GPe input following chronic 6-OHDA lesion? One possible explanation for the slow kinetics of the pallidostriatal response in SPNs (relative to INTs) is that it originates in the dendrites. If this is correct, then a shift in the location of the GPe-SPN synapses toward more proximal sites or even somatic regions would explain the increased amplitude of the IPSCs measured with patch electrodes at the soma following 6-OHDA lesion. To examine this possibility, we investigated the spatial relationship between GPe axons and SPN dendrites in *ex vivo* tissue slices using spinning-disk confocal microscopy. As illustrated in Figure 6, *a* and *b*, the apposition of GPe axons to dendrites of dSPNs and iSPNs was readily observed. By examining the branching structures of SPN dendrites, we discovered that ~90% of all GPe-SPN contacts were formed on the secondary, tertiary, and quaternary dendrites. Contacts in somatic regions and primary dendrites of SPNs were scarce (Fig. 6*c*).

Additionally, the positions of contacts made by GPe axons along the somatodendritic axis of SPNs were determined by their Euclidean distance from the soma (Fig. 6*d*). We found that GPe-iSPN contacts were located closer to the soma than GPe-dSPN contacts (dSPNs:  $52.0 \pm 10.4 \mu\text{m}$ ,  $n = 67$  contacts; iSPNs:  $39.9 \pm 15.0 \mu\text{m}$ ,  $n = 107$  contacts;  $p < 0.0001$ ), consistent with the larger pallidostriatal IPSCs in iSPNs relative to dSPNs. Furthermore, we observed that GPe-SPN contact locations were closer to the cell body of dSPNs following chronic 6-OHDA lesion (naïve:  $52.0 \pm 10.4 \mu\text{m}$ ,  $n = 67$  contacts; 6-OHDA:  $48.4 \pm 9.2 \mu\text{m}$ ,  $n = 18$  contacts;  $p = 0.0363$ ). This shift could explain the increase in the strength of the pallidostriatal response in dSPNs. In contrast, GPe-SPN contact locations were shifted away from the cell body of iSPNs following chronic 6-OHDA lesion (naïve:  $39.9 \pm 15.0 \mu\text{m}$ ,  $n = 107$  contacts; 6-OHDA:  $49.3 \pm 14.7 \mu\text{m}$ ,  $n = 38$  contacts;  $p = 0.0367$ ). This is unexpected given the enhancement of the pallidostriatal response amplitude observed in iSPNs following chronic 6-OHDA lesion.

Given the difference in the extent of the enhancement of the pallidostriatal IPSCs in dSPNs and iSPNs after chronic 6-OHDA lesion, we hypothesized that postsynaptic mechanisms, such as the upregulation of postsynaptic GABA<sub>A</sub> receptor expression, were involved. To this end, we performed qPCR analysis on FACS-purified dSPNs and iSPNs in naïve and chronic 6-OHDA-lesioned mice. This revealed that the transcript expression of different GABA<sub>A</sub> receptor subunits in dSPNs was either decreased or unaltered with chronic 6-OHDA lesion, further supporting our argument that the change in the location of the GPe synaptic contacts accounts for the increased GPe input to this cell type. In contrast, more complex changes were observed in iSPNs (Fig. 7*a*). The transcript abundance of different GABA<sub>A</sub> subunits in SPNs and their alterations following chronic 6-OHDA lesioning

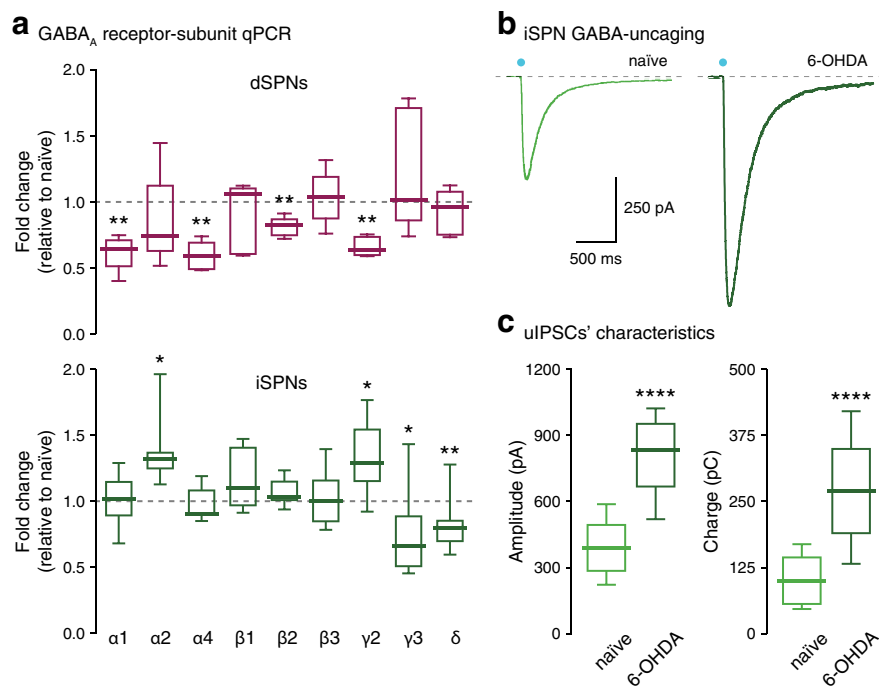


**Figure 7.** iSPNs have increased GABA<sub>A</sub> receptor surface expression following chronic 6-OHDA lesion. *a*, Transcript expression of different GABA<sub>A</sub> receptor subunits in dSPNs (top) and iSPNs (bottom) following chronic 6-OHDA lesion. Results are presented as fold differences relative to their respective naïve controls. Only data for  $\alpha 1$  (*Gabra1*),  $\alpha 2$  (*Gabra2*),  $\alpha 4$  (*Gabra1*),  $\beta 1$  (*Gabrb1*),  $\beta 2$  (*Gabrb2*),  $\beta 3$  (*Gabrb3*),  $\gamma 2$  (*Gabra2*),  $\gamma 3$  (*Gabra3*), and  $\delta$  (*Gabrd*) are included. No data for  $\alpha 3$  (*Gabra3*),  $\alpha 5$  (*Gabra5*), or  $\gamma 1$  (*Gabra1*) are presented as they have low or undetectable expression in SPNs. *b*, Representative GABA-uncaging responses (ulPSCs) in iSPNs from naïve (green, left) and chronic 6-OHDA lesioned (dark green, right) mice. *c*, Box plots summarizing the difference between naïve (green, left) and chronic 6-OHDA lesioned (dark green, right) mice in ulPSC amplitude (naïve:  $387.8 \pm 90.8$  pA,  $n = 22$  cells; 6-OHDA:  $832.6 \pm 110.1$  pA,  $n = 10$  cells;  $p < 0.0001$ , Mann–Whitney *U* test) and charge (naïve:  $99.3 \pm 42.9$  pC,  $n = 22$  cells; 6-OHDA:  $270.8 \pm 60.1$  pC,  $n = 10$  cells;  $p < 0.0001$ , Mann–Whitney *U* test). Medians  $\pm$  median absolute deviations and two-tailed *p* values are listed. Medians, interquartile ranges, and 10–90th percentiles are also presented in a graphic format. Asterisks denote statistical significance level (\* $p < 0.05$ , \*\* $p < 0.01$ , \*\*\*\* $p < 0.0001$ , Mann–Whitney *U* test and Wilcoxon signed rank test).

are listed in Table 3. Of note, the upregulation of  $\alpha 2$ -subunit ( $1.33 \pm 0.08$ -fold,  $p = 0.0330$ ) and  $\gamma 2$ -subunit ( $1.30 \pm 0.12$ -fold,  $p = 0.0031$ ) following chronic 6-OHDA lesion should promote surface—particularly synaptic—expression of GABA<sub>A</sub> receptors in iSPNs. Furthermore, we have previously demonstrated that an increase in the expression of the  $\gamma 2$ -subunit underlies the strengthening of the GPe-STN synapse following chronic 6-OHDA lesion (Fan et al., 2012). We used GABA uncaging to assess the total surface expression of GABA<sub>A</sub> receptors on iSPNs to avoid any confounding presynaptic factors that would affect the responses. Consistent with our hypothesis, chronic 6-OHDA lesion resulted in an approximately twofold increase in the uncaging response amplitude (naïve:  $387.8 \pm 90.8$  pA,  $n = 22$  cells; 6-OHDA:  $832.6 \pm 110.1$  pA,  $n = 10$  cells;  $p < 0.0001$ ) and net charge transfer (naïve:  $99.3 \pm 42.9$  pC,  $n = 22$  cells; 6-OHDA:  $270.8 \pm 60.1$  pC,  $n = 10$  cells;  $p < 0.0001$ ) following chronic 6-OHDA lesion (Fig. 7*b,c*). A modest but consistent increase in the uncaging responses was also found in dSPNs following chronic 6-OHDA lesion (naïve:  $307.4 \pm 113.3$  pA,  $n = 16$  cells; 6-OHDA:  $428.0 \pm 107.4$  pA,  $n = 10$  cells;  $p = 0.0467$ ; data not shown). The increase in the uncaging responses relative to the median of their respective naïve controls was larger in iSPNs than in dSPNs (dSPNs:  $1.39 \pm 0.35$ -fold,  $n = 10$  cells; iSPNs:  $2.15 \pm 0.28$ -fold,  $n = 10$  cells;  $p = 0.0354$ ). Altogether, these data support the involvement of postsynaptic mechanisms underlying



**Table 3. GABA<sub>A</sub> receptor-subunit transcript levels**

	dSPNs				iSPNs			
	Naïve ( $\Delta C_T$ , $n = 6$ )	6-OHDA ( $\Delta C_T$ , $n = 5$ )	Fold change ( $2^{-\Delta\Delta C_T}$ )	$p$ value*	Naïve ( $\Delta C_T$ , $n = 7$ )	6-OHDA ( $\Delta C_T$ , $n = 11$ )	Fold change ( $2^{-\Delta\Delta C_T}$ )	$p$ value*
GABA <sub>A</sub> $\alpha 1$	$-0.57 \pm 0.26$	$0.08 \pm 0.06$	$0.64 \pm 0.03$	<b>0.0022</b>	$-0.52 \pm 0.05$	$-0.55 \pm 0.17$	$1.02 \pm 0.12$	0.4705
GABA <sub>A</sub> $\alpha 2$	$2.17 \pm 0.24$	$2.54 \pm 0.28$	$0.77 \pm 0.14$	0.1797	$2.40 \pm 0.08$	$1.99 \pm 0.09$	$1.33 \pm 0.08$	<b>0.0330</b>
GABA <sub>A</sub> $\alpha 4$	$1.14 \pm 0.22$	$1.83 \pm 0.28$	$0.62 \pm 0.12$	<b>0.0087</b>	$1.09 \pm 0.16$	$1.14 \pm 0.11$	$0.97 \pm 0.07$	0.7806
GABA <sub>A</sub> $\beta 1$	$1.76 \pm 0.18$	$1.66 \pm 0.13$	$1.07 \pm 0.10$	0.8983	$1.98 \pm 0.10$	$1.87 \pm 0.17$	$1.08 \pm 0.12$	0.1609
GABA <sub>A</sub> $\beta 2$	$1.30 \pm 0.08$	$1.58 \pm 0.12$	$0.82 \pm 0.07$	<b>0.0087</b>	$1.24 \pm 0.06$	$1.16 \pm 0.09$	$1.06 \pm 0.06$	0.5309
GABA <sub>A</sub> $\beta 3$	$0.82 \pm 0.09$	$0.75 \pm 0.21$	$1.05 \pm 0.16$	0.4740	$0.88 \pm 0.05$	$0.92 \pm 0.21$	$0.97 \pm 0.13$	0.9252
GABA <sub>A</sub> $\gamma 2$	$1.43 \pm 0.11$	$1.99 \pm 0.16$	$0.68 \pm 0.07$	<b>0.0043</b>	$1.44 \pm 0.10$	$1.05 \pm 0.13$	$1.30 \pm 0.12$	<b>0.0031</b>
GABA <sub>A</sub> $\gamma 3$	$4.17 \pm 0.22$	$3.81 \pm 0.43$	$1.33 \pm 0.40$	0.3874	$3.64 \pm 0.12$	$4.26 \pm 0.37$	$0.65 \pm 0.18$	<b>0.0031</b>
GABA <sub>A</sub> $\delta$	$1.91 \pm 0.10$	$1.92 \pm 0.24$	$1.00 \pm 0.18$	0.8983	$2.08 \pm 0.04$	$2.41 \pm 0.11$	$0.79 \pm 0.06$	<b>0.0001</b>

Values are reported as the median  $\pm$  median absolute deviation.

\*Mann–Whitney test; two-tailed exact  $p$  values are shown.  $p$  values  $<0.05$  are shown in bold.

the increased pallidostriatal response amplitude in iSPNs in the chronic 6-OHDA lesioned mice.

### Activation of Npas1<sup>+</sup> GPe neurons suppresses motor output

The synaptic connections to SPNs suggest that Npas1<sup>+</sup> GPe neurons are important for motor function. This idea is consistent with findings in recent literature showing the correlation between movements and unit activity (Dodson et al., 2015; Mallet et al., 2016). To interrogate the role of Npas1<sup>+</sup> GPe neurons in motor output, a chemogenetic approach (Armbruster et al., 2007; Sternson and Roth, 2014) was used to selectively activate this neuronal population. The ambulatory activity of *Npas1-Cre* mice was assessed. Chemogenetic activation of designer receptors exclusively activated by designer drugs hM3Dq-expressing Npas1<sup>+</sup> GPe neurons with systemic administration of CNO (baseline,  $6.0 \pm 4.1$  s; CNO,  $26.4 \pm 5.6$  s; vehicle,  $17.0 \pm 4.5$  s;  $n = 9$  mice) increased the length of time that the mice spent motionless relative to baseline ( $p = 0.0273$ ; Fig. 8*b*). This effect was also different from vehicle control ( $p = 0.0039$ ). Control *Npas1-Cre* (baseline,  $10.2 \pm 10.2$  s; CNO,  $5.7 \pm 4.5$  s; vehicle,  $16.7 \pm 14.1$  s;  $n = 9$  mice) showed no responsiveness to systemic administration of CNO when compared with baseline values ( $p = 0.6406$ ) or with vehicle values ( $p = 0.1641$ ). Concordantly, the effect of CNO on time spent motionless was greater in *Npas1-Cre* mice with hM3Dq expression in the GPe than in control mice (controls:  $5.7 \pm 4.5$  s,  $n = 9$  mice; hM3Dq mice:  $26.4 \pm 5.6$  s,  $n = 9$  mice;  $p = 0.0056$ ).

### Discussion

An anatomical projection from the GPe to the dStr has been described for decades, but little is known about its connectivity pattern. In this study, we demonstrated that Npas1<sup>+</sup> neurons provide the principal GPe input to both dSPNs and iSPNs. Following chronic dopamine lesion, there is an enhancement of the GPe input to both dSPNs and iSPNs. While the strengthening of the GPe inputs to the dSPNs arise from an increase in proximal contacts, the strengthening of the GPe inputs to the iSPNs is likely a result of an increased postsynaptic GABA<sub>A</sub> receptor expression. Activation of the GPe inputs dampens the excitability of SPNs, especially in the chronic 6-OHDA lesioned state. Finally, chemogenetic activation of Npas1<sup>+</sup> GPe neurons increases the time that the mice spend motionless. Together, these data describe a novel inhibitory pathway of the basal ganglia relevant to motor function and dysfunction.

### Npas1<sup>+</sup> neurons constitute the principal GPe input to SPNs

Altogether, the axonal arborization pattern and cell-targeting properties of the Npas1<sup>+</sup> neurons are consistent with those of

“arkypallidal” GPe neurons (Mallet et al., 2012; Hegeman et al., 2016). The rabies-tracing experiments demonstrated a monosynaptic connection between PV<sup>−</sup> GPe neurons and SPNs (Fig. 3). While this corroborates our earlier findings (Hernández et al., 2015), it is at odds with those of a previous study (Wall et al., 2013) that showed no input from the GPe to SPNs using similar approaches. The reason for this discrepancy is unclear, but it may be due to nuanced differences in the viral preparations. Importantly, our development of the *Npas1-Cre* mouse (Hernández et al., 2015) enabled us to demonstrate that Npas1<sup>+</sup> GPe neurons constitute the principal pallidostriatal input to both dSPNs and iSPNs. In particular, IPSC characteristics of the Npas1<sup>+</sup> GPe-SPN input (Fig. 3) largely recapitulate those of the pan-GPe-SPN input (Table 2), including the increased strength of the GPe-SPN input in the chronic 6-OHDA lesioned condition (Fig. 5). In contrast, PV<sup>+</sup> neurons exhibit only limited connectivity to SPNs (Fig. 3).

Unlike PV<sup>+</sup> GPe neurons, which provide a strong input to the STN, Npas1<sup>+</sup> GPe neurons provide only a weak input to this nucleus, as indicated by the differing response amplitudes of these projections (Fig. 4). This further demonstrates that Npas1<sup>+</sup> GPe neurons exhibit the axonal arborization patterns of arkypallidal neurons (Mallet et al., 2012) and is consistent with previous findings that Foxp2 (a definitive marker for arkypallidal neurons) is expressed in the majority of Npas1<sup>+</sup> GPe neurons (Abdi et al., 2015; Dodson et al., 2015; Hernández et al., 2015). Given the ontogenic and molecular complexity of Npas1<sup>+</sup> neurons (Flanin et al., 2010; Nóbrega-Pereira et al., 2010; Abdi et al., 2015; Dodson et al., 2015; Hernández et al., 2015), it is possible that the STN-projecting Npas1<sup>+</sup> neurons are a subclass of Npas1<sup>+</sup> GPe neurons corresponding to the GPe neurons that have been shown to send axons both upstream to the dStr and downstream to the STN in single-neuron-tracing studies (Bevan et al., 1998; Sato et al., 2000; Fujiyama et al., 2015). It is worthwhile to note that the Lhx6-expressing (Lhx6<sup>+</sup>) population straddles multiple classes of GPe neurons (including both Npas1<sup>+</sup> neurons and PV<sup>+</sup> neurons) and does not correspond to the arkypallidal neurons (Gittis et al., 2014; Abdi et al., 2015; Dodson et al., 2015; Hernández et al., 2015; Hegeman et al., 2016). However, it remains to be seen whether Npas1<sup>+</sup>-Lhx6<sup>+</sup> GPe neurons correspond to this STN-projecting subclass of Npas1<sup>+</sup> GPe neurons. Moreover, our results further extend the observation that heterogeneity of GPe neuron projections exists within the STN (Xiao et al., 2015).

### Network activity and the GPe input in parkinsonian mice

There are several mechanisms by which Npas1<sup>+</sup> GPe input can control motor output. First, it has been shown that the activation of STN neurons is sufficient to stop action (Gittis et al., 2014). We

speculate that  $Npas1^{+}$  GPe neurons are downstream synaptic partners of the STN and that this connection serves to suppress competing motor programs. This idea is supported by computational modeling suggesting that pallidostriatal neurons are the primary postsynaptic partners of STN neurons (Nevado-Holgado et al., 2014). While “Stop” signals from the STN lead only to transient excitation of substantia nigra pars reticulata neurons, it is thought that an additional pathway must mediate the inhibition of “Go” signals for full behavioral stopping to occur (Schmidt et al., 2013). A recent study proposed that appropriately timed inhibition of the dStr by arky pallidal neurons may play a role in action suppression (Schmidt et al., 2013; Mallet et al., 2016). However, the postsynaptic partners and the properties of this connection were previously not known. Our present study provides the cellular correlates that mediate this signal—by inhibiting dSPNs (“Go” signals), the  $Npas1^{+}$  GPe input likely contributes to action suppression. On the other hand, the inhibition of iSPNs (“No-go” signals) by  $Npas1^{+}$  GPe neurons should facilitate action. It is now clear that coordinated activation of both dSPNs and iSPNs occurs during an action (Kravitz et al., 2010; Freeze et al., 2013; Calabresi et al., 2014; Sippy et al., 2015). However, additional mechanisms, such as neuromodulatory control, must exist to dictate the selective inhibition of dSPNs over iSPNs (and vice versa) by  $Npas1^{+}$  GPe neurons. The alterations in this neuromodulatory signal in PD may contribute to motor dysfunction.

In addition to action suppression,  $Npas1^{+}$  GPe neurons may serve as a gain control for the striatum. It has been previously demonstrated that a nonspecific inhibitory input can facilitate information processing in this manner (Laurent, 2002; Isaacson and Scanziani, 2011). It is appealing to propose that by projecting across a broad area of the striatum,  $Npas1^{+}$  GPe input has the potential to dampen the responses of large populations of unpreferred (i.e., weak) excitatory events onto SPNs, thus promoting the activity of SPNs that are receiving preferred (i.e., strong and well-timed) excitatory events (Burrone and Murthy, 2003; Semyanov et al., 2004; Silver, 2010; for further discussion, see Hegeman et al., 2016). Consistent with this idea,  $Npas1^{+}$  GPe input synapses preferentially on dendritic regions of both dSPNs and iSPNs. This synaptic organization is similar to that formed by the local collaterals of SPNs, but contrasts with the majority of the GABAergic inputs, which synapse onto the cell body and proximal dendrites of SPNs (Wilson, 2007; Sizemore et al., 2016). In the dopamine-depleted state, iSPNs exhibit selective enhancement of the strength of their excitatory cortical input (Day et al., 2006; Peterson et al., 2012). Under these conditions, the strengthened, dendritically targeted  $Npas1^{+}$  GPe input to iSPNs should counteract their increased excitatory cortical drive and correct aberrant network changes linked to motor symptoms in PD. However, as the strength of the  $Npas1^{+}$  GPe input to both dSPNs and iSPNs is increased following chronic 6-OHDA lesion (Fig. 5), it is not clear from a parallel pathway perspective whether the alterations are likely to be beneficial or maladaptive. On the other

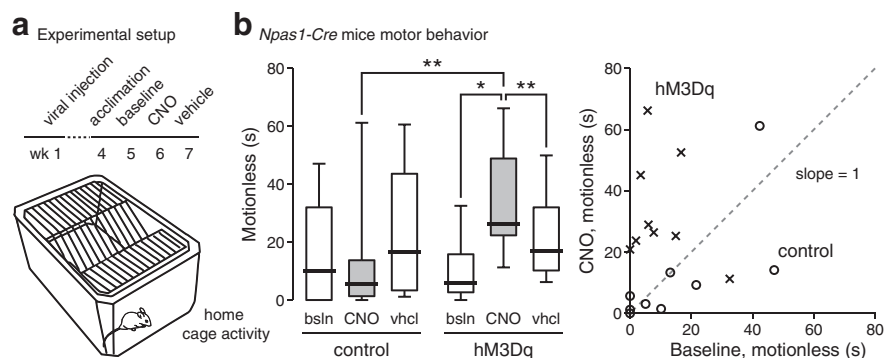


**Figure 8.** Activation of  $Npas1^{+}$  GPe neurons suppresses motor output. **a**, Experimental setup and timeline. Motor behavior assessed using an automated home cage scoring system. Subjects were repeatedly tested for 4 consecutive weeks at 1 week intervals. **b**, Left, Intraperitoneal injection of CNO (gray) did not alter the time spent motionless by control  $Npas1$ -Cre mice relative to baseline values ( $p = 0.6406$ , Wilcoxon signed rank test) or to vehicle values ( $p = 0.1641$ , Wilcoxon signed rank test; baseline:  $10.2 \pm 10.2$  s; CNO:  $5.7 \pm 4.5$  s; vehicle:  $16.7 \pm 14.1$  s;  $n = 9$  mice). The control group included two naïve  $Npas1$ -Cre mice and seven sham-injected  $Npas1$ -Cre mice. Intraperitoneal injection of CNO (gray) increased the length of time that the  $Npas1$ -Cre mice spent motionless with hM3Dq AAV infection in the GPe relative to baseline (baseline:  $6.0 \pm 4.1$  s; CNO:  $26.4 \pm 5.6$  s;  $n = 9$  mice;  $p = 0.0273$ , Wilcoxon signed rank test). This effect of CNO was reversible (CNO:  $26.4 \pm 5.6$  s; vehicle:  $17.0 \pm 4.5$  s;  $n = 9$  mice;  $p = 0.0039$ , Wilcoxon signed rank test) and was different from CNO in control  $Npas1$ -Cre mice ( $p = 0.0056$ , Mann–Whitney  $U$  test). Right, The effects of CNO on control mice (circles) and hM3Dq mice (crosses) are shown. Each symbol represents an individual mouse. Medians  $\pm$  median absolute deviations and two-tailed  $p$  values are listed. Medians, interquartile ranges, and 10–90th percentiles are also presented in a graphic format. Asterisks denote statistical significance level (\* $p < 0.05$ , \*\* $p < 0.01$ , Mann–Whitney  $U$  test and Wilcoxon signed rank test).

hand, as the coactivation of dSPNs and iSPNs is required to produce desired movements (Mink, 1996; Hikosaka et al., 2000; Cui et al., 2013; Tecuapetla et al., 2014), we propose that a reduction of the  $Npas1^{+}$  GPe input, which provides a spatially broad inhibition of both dSPNs and iSPNs across the dStr, is permissive to the initiation and execution of somatotopically complex motor sequences. Conversely, inappropriate strengthening of this  $Npas1^{+}$  GPe input to both dSPNs and iSPNs should suppress movements. This model is consistent with the finding that PD patients experience difficulty in performing volitional movements (Lang and Lozano, 1998; Dauer and Przedborski, 2003; Fahn, 2003; Redgrave et al., 2010). This idea is supported by the chemogenetic experiments in which the activation of  $Npas1^{+}$  GPe neurons increases the amount of time that the mice spend motionless (Fig. 8). However, further investigation is needed to confirm the precise role of  $Npas1^{+}$  GPe neurons in hypokinetic symptoms of PD.

Finally, along with targeting SPNs, this study and others have demonstrated that the pallidostriatal projection targets interneurons (Bevan et al., 1998; Mallet et al., 2012; Mastro et al., 2014; Saunders et al., 2016). As interneurons are central to network synchronization and rhythms (Freund, 2003; Berke et al., 2004; Bartos et al., 2007; Uhlhaas and Singer, 2010; Gittis et al., 2011; Allen and Monyer, 2015), future studies will be important to assess the functional alterations of the pallidostriatal input to different interneuron classes in parkinsonian conditions. These studies will help to delineate the contribution of the pallidostriatal input to the aberrant cross-coupling of different network-mediated oscillations in PD (López-Azcárate et al., 2010, 2013; Richardson, 2013; de Hemptinne et al., 2013; Yang et al., 2014). In particular, appropriate control of  $\beta$ -oscillations (13–30 Hz) is crucial for motor output. In contrast,  $\beta$ -oscillations are prevalent in PD, and their emergence correlates with the onset of hypokinetic symptoms (Kühn et al., 2004; Gatev et al., 2006; Little et al., 2012; Stein and Bar-Gad, 2013). Increased  $\beta$ -oscillations are observed in the dStr in parkinsonian conditions (Courtemanche et

al., 2003; Costa et al., 2006; Moran et al., 2011; Lemaire et al., 2012; Feingold et al., 2015). Computational models suggest that GABA<sub>A</sub> conductances in SPNs are important in regulating local membrane properties and, subsequently, the power of  $\beta$ -oscillations in the dStr (McCarthy et al., 2011; Damodaran et al., 2014, 2015). Our research findings suggest that the strengthened Npas1<sup>+</sup> GPe-SPN input may participate directly in the exaggerated  $\beta$ -oscillations or indirectly via altered tuning of the local collateral and interneuron inputs within the dStr.

## References

- Abdi A, Mallet N, Mohamed FY, Sharott A, Dodson PD, Nakamura KC, Suri S, Avery SV, Larvin JT, Garas FN, Garas SN, Vinciati F, Morin S, Bezard E, Baufreton J, Magill PJ (2015) Prototypic and arkypallidal neurons in the dopamine-intact external globus pallidus. *J Neurosci* 35:6667–6688. [CrossRef Medline](#)
- Abedi PM, Delaville C, De Deurwaerdere P, Benjelloun W, Benazzouz A (2013) Intrapallidal administration of 6-hydroxydopamine mimics in large part the electrophysiological and behavioral consequences of major dopamine depletion in the rat. *Neuroscience* 236:289–297. [CrossRef Medline](#)
- Albin RL, Young AB, Penney JB (1989) The functional anatomy of basal ganglia disorders. *Trends Neurosci* 12:366–375. [CrossRef Medline](#)
- Allen K, Monyer H (2015) Interneuron control of hippocampal oscillations. *Curr Opin Neurobiol* 31:81–87. [CrossRef Medline](#)
- Anderson ME, Horak FB (1985) Influence of the globus pallidus on arm movements in monkeys. III. Timing of movement-related information. *J Neurophysiol* 54:433–448. [Medline](#)
- Arkadir D, Morris G, Vaadia E, Bergman H (2004) Independent coding of movement direction and reward prediction by single pallidal neurons. *J Neurosci* 24:10047–10056. [CrossRef Medline](#)
- Armbruster BN, Li X, Pausch MH, Herlitze S, Roth BL (2007) Evolving the lock to fit the key to create a family of G protein-coupled receptors potentially activated by an inert ligand. *Proc Natl Acad Sci U S A* 104:5163–5168. [CrossRef Medline](#)
- Bartos M, Vida I, Jonas P (2007) Synaptic mechanisms of synchronized gamma oscillations in inhibitory interneuron networks. *Nat Rev Neurosci* 8:45–56. [CrossRef Medline](#)
- Beckstead RM (1983) A pallidostriatal projection in the cat and monkey. *Brain Res Bull* 11:629–632. [CrossRef Medline](#)
- Bergman H, Feingold A, Nini A, Raz A, Sloviter H, Abeles M, Vaadia E (1998) Physiological aspects of information processing in the basal ganglia of normal and parkinsonian primates. *Trends Neurosci* 21:32–38. [CrossRef Medline](#)
- Berke JD, Okatan M, Skurski J, Eichenbaum HB (2004) Oscillatory entrainment of striatal neurons in freely moving rats. *Neuron* 43:883–896. [CrossRef Medline](#)
- Bevan MD, Booth PA, Eaton SA, Bolam JP (1998) Selective innervation of neostriatal interneurons by a subclass of neuron in the globus pallidus of the rat. *J Neurosci* 18:9438–9452. [Medline](#)
- Bolam JP, Hanley JJ, Booth PA, Bevan MD (2000) Synaptic organization of the basal ganglia. *J Anat* 196:527–542. [CrossRef Medline](#)
- Burrone J, Murthy VN (2003) Synaptic gain control and homeostasis. *Curr Opin Neurobiol* 13:560–567. [CrossRef Medline](#)
- Calabresi P, Picconi B, Tozzi A, Ghiglieri V, Di Filippo M (2014) Direct and indirect pathways of basal ganglia: a critical reappraisal. *Nat Neurosci* 17:1022–1030. [CrossRef Medline](#)
- Callaway EM, Luo L (2015) Monosynaptic circuit tracing with glycoprotein-deleted rabies viruses. *J Neurosci* 35:8979–8985. [CrossRef Medline](#)
- Chan CS, Glajch KE, Gertler TS, Guzman JN, Mercer JN, Lewis AS, Goldberg AB, Tkatch T, Shigemoto R, Fleming SM, Chetkovich DM, Osten P, Kita H, Surmeier DJ (2011) HCN channelopathy in external globus pallidus neurons in models of Parkinson's disease. *Nat Neurosci* 14:85–92. [CrossRef Medline](#)
- Chan CS, Peterson JD, Gertler TS, Glajch KE, Quintana RE, Cui Q, Sebel LE, Plotkin JL, Shen W, Heiman M, Heintz N, Greengard P, Surmeier DJ (2012) Strain-specific regulation of striatal phenotype in Drd2-eGFP BAC transgenic mice. *J Neurosci* 32:9124–9132. [CrossRef Medline](#)
- Costa RM, Lin SC, Sotnikova TD, Cyr M, Gainetdinov RR, Caron MG, Nicolelis MA (2006) Rapid alterations in corticostriatal ensemble coordination during acute dopamine-dependent motor dysfunction. *Neuron* 52:359–369. [CrossRef Medline](#)
- Courtemanche R, Fujii N, Graybiel AM (2003) Synchronous, focally modulated beta-band oscillations characterize local field potential activity in the striatum of awake behaving monkeys. *J Neurosci* 23:11741–11752. [Medline](#)
- Cui G, Jun SB, Jin X, Pham MD, Vogel SS, Lovinger DM, Costa RM (2013) Concurrent activation of striatal direct and indirect pathways during action initiation. *Nature* 494:238–242. [CrossRef Medline](#)
- Damodaran S, Evans RC, Blackwell KT (2014) Synchronized firing of fast-spiking interneurons is critical to maintain balanced firing between direct and indirect pathway neurons of the striatum. *J Neurophysiol* 111:836–848. [CrossRef Medline](#)
- Damodaran S, Cressman JR, Jedrzejewski-Szmek Z, Blackwell KT (2015) Desynchronization of fast-spiking interneurons reduces beta-band oscillations and imbalance in firing in the dopamine-depleted striatum. *J Neurosci* 35:1149–1159. [CrossRef Medline](#)
- Dauer W, Przedborski S (2003) Parkinson's disease: mechanisms and models. *Neuron* 39:889–909. [CrossRef Medline](#)
- Day M, Wang Z, Ding J, An X, Ingham CA, Shering AF, Wokosin D, Ilijic E, Sun Z, Sampson AR, Mugnaini E, Deutch AY, Sesack SR, Arbuthnott GW, Surmeier DJ (2006) Selective elimination of glutamatergic synapses on striatopallidal neurons in Parkinson disease models. *Nat Neurosci* 9:251–259. [CrossRef Medline](#)
- de Hemptinne C, Ryapolova-Webb ES, Air EL, Garcia PA, Miller KJ, Ojemann JG, Ostrem JL, Galifianakis NB, Starr PA (2013) Exaggerated phase-amplitude coupling in the primary motor cortex in Parkinson disease. *Proc Natl Acad Sci U S A* 110:4780–4785. [CrossRef Medline](#)
- DeLong MR (1971) Activity of pallidal neurons during movement. *J Neurophysiol* 34:414–427. [Medline](#)
- DeLong MR (1990) Primate models of movement disorders of basal ganglia origin. *Trends Neurosci* 13:281–285. [CrossRef Medline](#)
- Deng Y, Lanciego J, Goff LK, Coulon P, Salin P, Kachidian P, Lei W, Del Mar N, Reiner A (2015) Differential organization of cortical inputs to striatal projection neurons of the matrix compartment in rats. *Front Syst Neurosci* 9:51. [CrossRef Medline](#)
- Dodson PD, Larvin JT, Duffell JM, Garas FN, Doig NM, Kessaris N, Duguid IC, Bogacz R, Butt SJ, Magill PJ (2015) Distinct developmental origins manifest in the specialized encoding of movement by adult neurons of the external globus pallidus. *Neuron* 86:501–513. [CrossRef Medline](#)
- Fahn S (2003) Description of Parkinson's disease as a clinical syndrome. *Ann N Y Acad Sci* 991:1–14. [CrossRef Medline](#)
- Fahn S, Côté LJ (1968) Regional distribution of gamma-aminobutyric acid (GABA) in brain of the rhesus monkey. *J Neurochem* 15:209–213. [CrossRef Medline](#)
- Fan KY, Baufreton J, Surmeier DJ, Chan CS, Bevan MD (2012) Proliferation of external globus pallidus-subthalamic nucleus synapses following degeneration of midbrain dopamine neurons. *J Neurosci* 32:13718–13728. [CrossRef Medline](#)
- Feingold J, Gibson DJ, DePasquale B, Graybiel AM (2015) Bursts of beta oscillation differentiate postperformance activity in the striatum and motor cortex of monkeys performing movement tasks. *Proc Natl Acad Sci U S A* 112:13687–13692. [CrossRef Medline](#)
- Fieblinger T, Graves SM, Sebel LE, Alcacer C, Plotkin JL, Gertler TS, Chan CS, Heiman M, Greengard P, Cenci MA, Surmeier DJ (2014) Cell type-specific plasticity of striatal projection neurons in parkinsonism and L-DOPA-induced dyskinesia. *Nat Commun* 5:5316. [CrossRef Medline](#)
- Filion M, Tremblay L (1991) Abnormal spontaneous activity of globus pallidus neurons in monkeys with MPTP-induced parkinsonism. *Brain Res* 547:142–151. [Medline](#)
- Fisher RS, Boylan MK, Hull CD, Buchwald NA, Levine MS (1985) Branched projections of pallidal and peripallidal neurons to neocortex and neostriatum: a double-labeling study in the cat. *Brain Res* 326:156–159. [CrossRef Medline](#)
- Flandin P, Kimura S, Rubenstein JL (2010) The progenitor zone of the ventral medial ganglionic eminence requires Nkx2-1 to generate most of the globus pallidus but few neocortical interneurons. *J Neurosci* 30:2812–2823. [CrossRef Medline](#)
- Freeze BS, Kravitz AV, Hammack N, Berke JD, Kreitzer AC (2013) Control of basal ganglia output by direct and indirect pathway projection neurons. *J Neurosci* 33:18531–18539. [CrossRef Medline](#)



- Freund TF (2003) Interneuron diversity series: rhythm and mood in perisomatic inhibition. *Trends Neurosci* 26:489–495. [CrossRef Medline](#)
- Fujiyama F, Nakano T, Matsuda W, Furuta T, Udagawa J, Kaneko T (2015) A single-neuron tracing study of arky pallidal and prototypic neurons in healthy rats. *Brain Struct Funct*. Advance online publication. Retrieved April 6, 2016. doi:10.1007/s00429-015-1152-2. [CrossRef Medline](#)
- Gatev P, Darbin O, Wichmann T (2006) Oscillations in the basal ganglia under normal conditions and in movement disorders. *Mov Disord* 21:1566–1577. [CrossRef Medline](#)
- Gerfen CR, Paletzki R, Heintz N (2013) GENSAT BAC cre-recombinase driver lines to study the functional organization of cerebral cortical and basal ganglia circuits. *Neuron* 80:1368–1383. [CrossRef Medline](#)
- Gertler TS, Chan CS, Surmeier DJ (2008) Dichotomous anatomical properties of adult striatal medium spiny neurons. *J Neurosci* 28:10814–10824. [CrossRef Medline](#)
- Ghanem A, Conzelmann KK (2016) G gene-deficient single-round rabies viruses for neuronal circuit analysis. *Virus Res* 216:41–54. [CrossRef Medline](#)
- Gittis AH, Kreitzer AC (2012) Striatal microcircuitry and movement disorders. *Trends Neurosci* 35:557–564. [CrossRef Medline](#)
- Gittis AH, Hang GB, LaDow ES, Shoenfeld LR, Atallah BV, Finkbeiner S, Kreitzer AC (2011) Rapid target-specific remodeling of fast-spiking inhibitory circuits after loss of dopamine. *Neuron* 71:858–868. [CrossRef Medline](#)
- Gittis AH, Berke JD, Bevan MD, Chan CS, Mallet N, Morrow MM, Schmidt R (2014) New roles for the external globus pallidus in basal ganglia circuits and behavior. *J Neurosci* 34:15178–15183. [CrossRef Medline](#)
- Glajch KE, Fleming SM, Surmeier DJ, Osten P (2012) Sensorimotor assessment of the unilateral 6-hydroxydopamine mouse model of Parkinson's disease. *Behav Brain Res* 230:309–316. [CrossRef Medline](#)
- Gong S, Zheng C, Doughty ML, Losos K, Didkovsky N, Schambra UB, Nowak NJ, Joyner A, Leblanc G, Hatten ME, Heintz N (2003) A gene expression atlas of the central nervous system based on bacterial artificial chromosomes. *Nature* 425:917–925. [CrossRef Medline](#)
- Gritti I, Henny P, Galloni F, Mainville L, Mariotti M, Jones BE (2006) Stereological estimates of the basal forebrain cell population in the rat, including neurons containing choline acetyltransferase, glutamic acid decarboxylase or phosphate-activated glutaminase and colocalizing vesicular glutamate transporters. *Neuroscience* 143:1051–1064. [CrossRef Medline](#)
- Guo Q, Wang D, He X, Feng Q, Lin R, Xu F, Fu L, Luo M (2015) Whole-brain mapping of inputs to projection neurons and cholinergic interneurons in the dorsal striatum. *PLoS One* 10:e0123381. [CrossRef Medline](#)
- Hauber W (1998) Involvement of basal ganglia transmitter systems in movement initiation. *Prog Neurobiol* 56:507–540. [CrossRef Medline](#)
- Hauber W, Lutz S, Munkle M (1998) The effects of globus pallidus lesions on dopamine-dependent motor behaviour in rats. *Neuroscience* 86:147–157. [CrossRef Medline](#)
- Hegeman DJ, Hong ES, Hernández VM, Chan SC (2016) The external globus pallidus: progress and perspectives. *Eur J Neurosci*. Advance online publication. Retrieved April 6, 2016. doi:10.1111/ejn.13196. [CrossRef Medline](#)
- Hernández VM, Hegeman DJ, Cui Q, Kelver DA, Fiske MP, Glajch KE, Pitt JE, Huang TY, Justice NJ, Chan CS (2015) Parvalbumin+ neurons and Npas1+ neurons are distinct neuron classes in the mouse external globus pallidus. *J Neurosci* 35:11830–11847. [CrossRef Medline](#)
- Heuer A, Smith GA, Lelos MJ, Lane EL, Dunnett SB (2012) Unilateral nigrostriatal 6-hydroxydopamine lesions in mice I: motor impairments identify extent of dopamine depletion at three different lesion sites. *Behav Brain Res* 228:30–43. [CrossRef Medline](#)
- Hikosaka O, Takikawa Y, Kawagoe R (2000) Role of the basal ganglia in the control of purposive saccadic eye movements. *Physiol Rev* 80:953–978. [Medline](#)
- Hippenmeyer S, Vrieseling E, Sigrist M, Portmann T, Laengle C, Ladle DR, Arber S (2005) A developmental switch in the response of DRG neurons to ETS transcription factor signaling. *PLoS Biol* 3:e159. [CrossRef Medline](#)
- Hoover BR, Marshall JF (1999) Population characteristics of preproenkephalin mRNA-containing neurons in the globus pallidus of the rat. *Neurosci Lett* 265:199–202. [CrossRef Medline](#)
- Hoover BR, Marshall JF (2002) Further characterization of preproenkephalin mRNA-containing cells in the rodent globus pallidus. *Neuroscience* 111:111–125. [CrossRef Medline](#)
- Isaacson JS, Scanziani M (2011) How inhibition shapes cortical activity. *Neuron* 72:231–243. [CrossRef Medline](#)
- Jaeger D, Gilman S, Aldridge JW (1995) Neuronal activity in the striatum and pallidum of primates related to the execution of externally cued reaching movements. *Brain Res* 694:111–127. [CrossRef Medline](#)
- Jayaraman A (1983) Topographic organization and morphology of peripallidal and pallidal cells projecting to the striatum in cats. *Brain Res* 275:279–286. [CrossRef Medline](#)
- Jessell TM, Emson PC, Paxinos G, Cuello AC (1978) Topographic projections of substance P and GABA pathways in the striato- and pallido-nigral system: a biochemical and immunohistochemical study. *Brain Res* 152:487–498. [CrossRef Medline](#)
- Jin X, Tecuapetla F, Costa RM (2014) Basal ganglia subcircuits distinctively encode the parsing and concatenation of action sequences. *Nat Neurosci* 17:423–430. [CrossRef Medline](#)
- Johnson MD, Zhang J, Ghosh D, McIntyre CC, Vitek JL (2012) Neural targets for relieving parkinsonian rigidity and bradykinesia with pallidal deep brain stimulation. *J Neurophysiol* 108:567–577. [CrossRef Medline](#)
- Kim EJ, Juavinett AL, Kyubwa EM, Jacobs MW, Callaway EM (2015) Three types of cortical layer 5 neurons that differ in brain-wide connectivity and function. *Neuron* 88:1253–1267. [CrossRef Medline](#)
- Kimura M, Kato M, Shimazaki H, Watanabe K, Matsumoto N (1996) Neural information transferred from the putamen to the globus pallidus during learned movement in the monkey. *J Neurophysiol* 76:3771–3786. [Medline](#)
- Kita H (2007) Globus pallidus external segment. *Prog Brain Res* 160:111–133. [CrossRef Medline](#)
- Kita H, Kita T (2001) Number, origins, and chemical types of rat pallidostriatal projection neurons. *J Comp Neurol* 437:438–448. [CrossRef Medline](#)
- Kita H, Kitai ST (1991) Intracellular study of rat globus pallidus neurons: membrane properties and responses to neostriatal, subthalamic and nigral stimulation. *Brain Res* 564:296–305. [CrossRef Medline](#)
- Kita H, Tokuno H, Nambu A (1999) Monkey globus pallidus external segment neurons projecting to the neostriatum. *Neuroreport* 10:1467–1472. [CrossRef Medline](#)
- Klaus A, Planert H, Hjorth JJ, Berke JD, Silberberg G, Kotaleski JH (2011) Striatal fast-spiking interneurons: from firing patterns to postsynaptic impact. *Front Syst Neurosci* 5:57. [CrossRef Medline](#)
- Koós T, Tepper JM (2002) Dual cholinergic control of fast-spiking interneurons in the neostriatum. *J Neurosci* 22:529–535. [Medline](#)
- Kravitz AV, Freeze BS, Parker PR, Kay K, Thwin MT, Deisseroth K, Kreitzer AC (2010) Regulation of parkinsonian motor behaviours by optogenetic control of basal ganglia circuitry. *Nature* 466:622–626. [CrossRef Medline](#)
- Kreitzer AC (2009) Physiology and pharmacology of striatal neurons. *Annu Rev Neurosci* 32:127–147. [CrossRef Medline](#)
- Kreitzer AC, Malenka RC (2007) Endocannabinoid-mediated rescue of striatal LTD and motor deficits in Parkinson's disease models. *Nature* 445:643–647. [CrossRef Medline](#)
- Krzywinski M, Altman N (2014) Visualizing samples with box plots. *Nat Methods* 11:119–120. [CrossRef Medline](#)
- Kühn AA, Williams D, Kupsch A, Limousin P, Hariz M, Schneider GH, Yarrow K, Brown P (2004) Event-related beta desynchronization in human subthalamic nucleus correlates with motor performance. *Brain* 127:735–746. [CrossRef Medline](#)
- Lang AE, Lozano AM (1998) Parkinson's disease. First of two parts. *N Engl J Med* 339:1044–1053. [CrossRef Medline](#)
- Laurent G (2002) Olfactory network dynamics and the coding of multidimensional signals. *Nat Rev Neurosci* 3:884–895. [CrossRef Medline](#)
- Lemairé N, Hernandez LF, Hu D, Kubota Y, Howe MW, Graybiel AM (2012) Effects of dopamine depletion on LFP oscillations in striatum are task- and learning-dependent and selectively reversed by L-DOPA. *Proc Natl Acad Sci U S A* 109:18126–18131. [CrossRef Medline](#)
- Little S, Pogossyan A, Kuhn AA, Brown P (2012) beta band stability over time correlates with parkinsonian rigidity and bradykinesia. *Exp Neurol* 236:383–388. [CrossRef Medline](#)
- López-Azcárate J, Tainta M, Rodríguez-Oroz MC, Valencia M, González R, Guridi J, Iriarte J, Obeso JA, Artieda J, Alegre M (2010) Coupling between beta and high-frequency activity in the human subthalamic nucleus may be a pathophysiological mechanism in Parkinson's disease. *J Neurosci* 30:6667–6677. [CrossRef Medline](#)

- López-Azcárate J, Nicolás MJ, Cordon I, Alegre M, Valencia M, Artieda J (2013) Delta-mediated cross-frequency coupling organizes oscillatory activity across the rat cortico-basal ganglia network. *Front Neural Circuits* 7:155. [CrossRef Medline](#)
- Mallet N, Pogosyan A, Márton LF, Bolam JP, Brown P, Magill PJ (2008) Parkinsonian beta oscillations in the external globus pallidus and their relationship with subthalamic nucleus activity. *J Neurosci* 28:14245–14258. [CrossRef Medline](#)
- Mallet N, Micklem BR, Henny P, Brown MT, Williams C, Bolam JP, Nakamura KC, Magill PJ (2012) Dichotomous organization of the external globus pallidus. *Neuron* 74:1075–1086. [CrossRef Medline](#)
- Mallet N, Schmidt R, Leventhal D, Chen F, Amer N, Boraud T, Berke JD (2016) Arkypallidal cells send a stop signal to striatum. *Neuron* 89:308–316. [CrossRef Medline](#)
- Mastro KJ, Bouchard RS, Holt HA, Gittis AH (2014) Transgenic mouse lines subdivide external segment of the globus pallidus (GPe) neurons and reveal distinct GPe output pathways. *J Neurosci* 34:2087–2099. [CrossRef Medline](#)
- McCarthy MM, Moore-Kochlacs C, Gu X, Boyden ES, Han X, Kopell N (2011) Striatal origin of the pathologic beta oscillations in Parkinson's disease. *Proc Natl Acad Sci U S A* 108:11620–11625. [CrossRef Medline](#)
- McGeorge AJ, Faull RL (1989) The organization of the projection from the cerebral cortex to the striatum in the rat. *Neuroscience* 29:503–537. [CrossRef Medline](#)
- Mink JW (1996) The basal ganglia: focused selection and inhibition of competing motor programs. *Prog Neurobiol* 50:381–425. [CrossRef Medline](#)
- Mitchell SJ, Richardson RT, Baker FH, DeLong MR (1987) The primate globus pallidus: neuronal activity related to direction of movement. *Exp Brain Res* 68:491–505. [Medline](#)
- Moran RJ, Mallet N, Litvak V, Dolan RJ, Magill PJ, Friston KJ, Brown P (2011) Alterations in brain connectivity underlying beta oscillations in Parkinsonism. *PLoS Comput Biol* 7:e1002124. [CrossRef Medline](#)
- Nambu A, Llinás R (1997) Morphology of globus pallidus neurons: its correlation with electrophysiology in guinea pig brain slices. *J Comp Neurol* 377:85–94. [CrossRef Medline](#)
- Nambu A, Tokuno H, Takada M (2002) Functional significance of the cortico-subthalamo-pallidal “hyperdirect” pathway. *Neurosci Res* 43:111–117. [CrossRef Medline](#)
- Nauta HJ (1979) Projections of the pallidal complex: an autoradiographic study in the cat. *Neuroscience* 4:1853–1873. [CrossRef Medline](#)
- Nevado-Holgado AJ, Mallet N, Magill PJ, Bogacz R (2014) Effective connectivity of the subthalamic nucleus-globus pallidus network during parkinsonian oscillations. *J Physiol* 592:1429–1455. [CrossRef Medline](#)
- Nóbrega-Pereira S, Gelman D, Bartolini G, Pla R, Pierani A, Marín O (2010) Origin and molecular specification of globus pallidus neurons. *J Neurosci* 30:2824–2834. [CrossRef Medline](#)
- Obeso JA, Rodríguez-Oroz MC, Javier Blesa F, Guridi J (2006) The globus pallidus pars externa and Parkinson's disease. Ready for prime time? *Exp Neurol* 202:1–7. [CrossRef Medline](#)
- Oertel WH, Mugnaini E (1984) Immunocytochemical studies of GABAergic neurons in rat basal ganglia and their relations to other neuronal systems. *Neurosci Lett* 47:233–238. [CrossRef Medline](#)
- Oertel WH, Nitsch C, Mugnaini E (1984) Immunocytochemical demonstration of the GABA-ergic neurons in rat globus pallidus and nucleus entopeduncularis and their GABA-ergic innervation. *Adv Neurol* 40:91–98. [Medline](#)
- Parent A, Hazrati LN (1995) Functional anatomy of the basal ganglia. I. The cortico-basal ganglia-thalamo-cortical loop. *Brain Res Brain Res Rev* 20:91–127. [CrossRef Medline](#)
- Peterson JD, Goldberg JA, Surmeier DJ (2012) Adenosine A2a receptor antagonists attenuate striatal adaptations following dopamine depletion. *Neurobiol Dis* 45:409–416. [CrossRef Medline](#)
- Petreanu L, Mao T, Sternson SM, Svoboda K (2009) The subcellular organization of neocortical excitatory connections. *Nature* 457:1142–1145. [CrossRef Medline](#)
- Plotkin JL, Shen W, Rafalovich I, Sebel LE, Day M, Chan CS, Surmeier DJ (2013) Regulation of dendritic calcium release in striatal spiny projection neurons. *J Neurophysiol* 110:2325–2336. [CrossRef Medline](#)
- Plotkin JL, Day M, Peterson JD, Xie Z, Kress GJ, Rafalovich I, Kondapalli J, Gertler TS, Flajolet M, Greengard P, Stavarache M, Kaplitt MG, Rosinski J, Chan CS, Surmeier DJ (2014) Impaired TrkB receptor signaling underlies corticostriatal dysfunction in Huntington's disease. *Neuron* 83:178–188. [CrossRef Medline](#)
- Rajakumar N, Elisevich K, Flumerfelt BA (1994) The pallidostriatal projection in the rat: a recurrent inhibitory loop? *Brain Res* 651:332–336. [CrossRef Medline](#)
- Rajput AH, Sitte HH, Rajput A, Fenton ME, Pifl C, Hornykiewicz O (2008) Globus pallidus dopamine and Parkinson motor subtypes: clinical and brain biochemical correlation. *Neurology* 70:1403–1410. [CrossRef Medline](#)
- Raz A, Vaadia E, Bergman H (2000) Firing patterns and correlations of spontaneous discharge of pallidal neurons in the normal and the tremulous 1-methyl-4-phenyl-1,2,3,6-tetrahydropyridine vervet model of parkinsonism. *J Neurosci* 20:8559–8571. [Medline](#)
- Reardon TR, Murray AJ, Turi GF, Wirblich C, Croce KR, Schnell MJ, Jessell TM, Losonczy A (2016) Rabies virus CVS-N2c strain enhances retrograde synaptic transfer and neuronal viability. *Neuron* 89:711–724. [CrossRef Medline](#)
- Redgrave P, Rodríguez M, Smith Y, Rodríguez-Oroz MC, Lehericy S, Bergman H, Agid Y, DeLong MR, Obeso JA (2010) Goal-directed and habitual control in the basal ganglia: implications for Parkinson's disease. *Nat Rev Neurosci* 11:760–772. [CrossRef Medline](#)
- Richardson RM (2013) Abnormal cortical brain rhythms in Parkinson disease. *Neurosurgery* 72:N23–N24. [CrossRef Medline](#)
- Sato F, Lavallée P, Lévesque M, Parent A (2000) Single-axon tracing study of neurons of the external segment of the globus pallidus in primate. *J Comp Neurol* 417:17–31. [CrossRef Medline](#)
- Saunders A, Oldenburg IA, Berezovskii VK, Johnson CA, Kingery ND, Elliott HL, Xie T, Gerfen CR, Sabatini BL (2015) A direct GABAergic output from the basal ganglia to frontal cortex. *Nature* 521:85–89. [CrossRef Medline](#)
- Saunders A, Huang KW, Sabatini BL (2016) Globus pallidus externus neurons expressing parvalbumin interconnect the subthalamic nucleus and striatal interneurons. *PLoS One* 11:e0149798. [CrossRef Medline](#)
- Schallert T, Fleming SM, Leasure JL, Tillerson JL, Bland ST (2000) CNS plasticity and assessment of forelimb sensorimotor outcome in unilateral rat models of stroke, cortical ablation, parkinsonism and spinal cord injury. *Neuropharmacology* 39:777–787. [CrossRef Medline](#)
- Schindelin J, Arganda-Carreras I, Frise E, Kaynig V, Longair M, Pietzsch T, Preibisch S, Rueden C, Saalfeld S, Schmid B, Tinevez JY, White DJ, Hartenstein V, Eliceiri K, Tomancak P, Cardona A (2012) Fiji: an open-source platform for biological-image analysis. *Nat Methods* 9:676–682. [CrossRef Medline](#)
- Schmidt R, Leventhal DK, Mallet N, Chen F, Berke JD (2013) Canceling actions involves a race between basal ganglia pathways. *Nat Neurosci* 16:1118–1124. [CrossRef Medline](#)
- Semyanov A, Walker MC, Kullmann DM, Silver RA (2004) Tonically active GABA A receptors: modulating gain and maintaining the tone. *Trends Neurosci* 27:262–269. [CrossRef Medline](#)
- Shammah-Lagnado SJ, Alheid GF, Heimer L (1996) Efferent connections of the caudal part of the globus pallidus in the rat. *J Comp Neurol* 376:489–507. [CrossRef Medline](#)
- Sheets PL, Suter BA, Kiritani T, Chan CS, Surmeier DJ, Shepherd GM (2011) Corticospinal-specific HCN expression in mouse motor cortex: I(h)-dependent synaptic integration as a candidate microcircuit mechanism involved in motor control. *J Neurophysiol* 106:2216–2231. [CrossRef Medline](#)
- Shinonaga Y, Takada M, Ogawa-Meguro R, Ikai Y, Mizuno N (1992) Direct projections from the globus pallidus to the midbrain and pons in the cat. *Neurosci Lett* 135:179–183. [CrossRef Medline](#)
- Shu SY, Peterson GM (1988) Anterograde and retrograde axonal transport of Phaseolus vulgaris leucoagglutinin (PHA-L) from the globus pallidus to the striatum of the rat. *J Neurosci Methods* 25:175–180. [CrossRef Medline](#)
- Shuen JA, Chen M, Gloss B, Calakos N (2008) Drd1a-tdTomato BAC transgenic mice for simultaneous visualization of medium spiny neurons in the direct and indirect pathways of the basal ganglia. *J Neurosci* 28:2681–2685. [CrossRef Medline](#)
- Silver RA (2010) Neuronal arithmetic. *Nat Rev Neurosci* 11:474–489. [CrossRef Medline](#)
- Sippy T, Lapray D, Crochet S, Petersen CC (2015) Cell-type-specific sensorimotor processing in striatal projection neurons during goal-directed behavior. *Neuron* 88:298–305. [CrossRef Medline](#)

- Sizemore RJ, Zhang R, Lin N, Goddard L, Wastney T, Parr-Brownlie LC, Reynolds JN, Oorschot DE (2016) Marked differences in the number and type of synapses innervating the somata and primary dendrites of midbrain dopaminergic neurons, striatal cholinergic interneurons, and striatal spiny projection neurons in the rat. *J Comp Neurol* 524:1062–1080. [CrossRef Medline](#)
- Smith Y, Parent A (1986) Differential connections of caudate nucleus and putamen in the squirrel monkey (*Saimiri sciureus*). *Neuroscience* 18:347–371. [CrossRef Medline](#)
- Spooren WP, Lynd-Balta E, Mitchell S, Haber SN (1996) Ventral pallidostriatal pathway in the monkey: evidence for modulation of basal ganglia circuits. *J Comp Neurol* 370:295–312. [CrossRef Medline](#)
- Staines WA, Fibiger HC (1984) Collateral projections of neurons of the rat globus pallidus to the striatum and substantia nigra. *Exp Brain Res* 56:217–220. [Medline](#)
- Staines WA, Atmadja S, Fibiger HC (1981) Demonstration of a pallidostriatal pathway by retrograde transport of HRP-labeled lectin. *Brain Res* 206:446–450. [CrossRef Medline](#)
- Stein E, Bar-Gad I (2013) beta oscillations in the cortico-basal ganglia loop during parkinsonism. *Exp Neurol* 245:52–59. [CrossRef Medline](#)
- Sternson SM, Roth BL (2014) Chemogenetic tools to interrogate brain functions. *Annu Rev Neurosci* 37:387–407. [CrossRef Medline](#)
- Streit M, Gehlenborg N (2014) Bar charts and box plots. *Nat Methods* 11:117. [CrossRef Medline](#)
- Tachibana Y, Iwamuro H, Kita H, Takada M, Nambu A (2011) Subthalamo-pallidal interactions underlying parkinsonian neuronal oscillations in the primate basal ganglia. *Eur J Neurosci* 34:1470–1484. [CrossRef Medline](#)
- Takada M, Ng G, Hattori T (1986) Single pallidal neurons project both to the striatum and thalamus in the rat. *Neurosci Lett* 69:217–220. [CrossRef Medline](#)
- Tecuapetla F, Matias S, Dugue GP, Mainen ZF, Costa RM (2014) Balanced activity in basal ganglia projection pathways is critical for contraversive movements. *Nat Commun* 5:4315. [CrossRef Medline](#)
- Tepper JM, Bolam JP (2004) Functional diversity and specificity of neostriatal interneurons. *Curr Opin Neurobiol* 14:685–692. [CrossRef Medline](#)
- Tepper JM, Wilson CJ, Koós T (2008) Feedforward and feedback inhibition in neostriatal GABAergic spiny neurons. *Brain Res Rev* 58:272–281. [CrossRef Medline](#)
- Tepper JM, Tecuapetla F, Koós T, Ibáñez-Sandoval O (2010) Heterogeneity and diversity of striatal GABAergic interneurons. *Front Neuroanat* 4:150. [CrossRef Medline](#)
- Tkatch T, Baranauskas G, Surmeier DJ (1998) Basal forebrain neurons adjacent to the globus pallidus co-express GABAergic and cholinergic marker mRNAs. *Neuroreport* 9:1935–1939. [CrossRef Medline](#)
- Turner RS, Anderson ME (2005) Context-dependent modulation of movement-related discharge in the primate globus pallidus. *J Neurosci* 25:2965–2976. [CrossRef Medline](#)
- Ugolini G (2011) Rabies virus as a transneuronal tracer of neuronal connections. *Adv Virus Res* 79:165–202. [CrossRef Medline](#)
- Uhlhaas PJ, Singer W (2010) Abnormal neural oscillations and synchrony in schizophrenia. *Nat Rev Neurosci* 11:100–113. [CrossRef Medline](#)
- Van de Weerd HA, Bulthuis RJ, Bergman AF, Schlingmann F, Tolboom J, Van Loo PL, Remie R, Baumanns V, Van Zutphen LF (2001) Validation of a new system for the automatic registration of behaviour in mice and rats. *Behav Processes* 53:11–20. [CrossRef Medline](#)
- Vitek JL, Hashimoto T, Peoples J, DeLong MR, Bakay RA (2004) Acute stimulation in the external segment of the globus pallidus improves parkinsonian motor signs. *Mov Disord* 19:907–915. [CrossRef Medline](#)
- Vitek JL, Zhang J, Hashimoto T, Russo GS, Baker KB (2012) External pallidal stimulation improves parkinsonian motor signs and modulates neuronal activity throughout the basal ganglia thalamic network. *Exp Neurol* 233:581–586. [CrossRef Medline](#)
- Walker RH, Arbutnot GW, Wright AK (1989) Electrophysiological and anatomical observations concerning the pallidostriatal pathway in the rat. *Exp Brain Res* 74:303–310. [Medline](#)
- Wall NR, De La Parra M, Callaway EM, Kreitzer AC (2013) Differential innervation of direct- and indirect-pathway striatal projection neurons. *Neuron* 79:347–360. [CrossRef Medline](#)
- Wilson CJ (2007) GABAergic inhibition in the neostriatum. *Prog Brain Res* 160:91–110. [CrossRef Medline](#)
- Wilson SK (1911) Progressive lenticular degeneration: a familial nervous disease associated with cirrhosis of the liver. *Brain* 34:205–502.
- Wilson SK (1913) An experimental research into the anatomy and physiology of the corpus striatum. *Brain* 36:427–492.
- Xiao C, Miwa JM, Henderson BJ, Wang Y, Deshpande P, McKinney SL, Lester HA (2015) Nicotinic receptor subtype-selective circuit patterns in the subthalamic nucleus. *J Neurosci* 35:3734–3746. [CrossRef Medline](#)
- Yang AI, Vanegas N, Lungu C, Zaghloul KA (2014) Beta-coupled high-frequency activity and beta-locked neuronal spiking in the subthalamic nucleus of Parkinson's disease. *J Neurosci* 34:12816–12827. [CrossRef Medline](#)
- Yoshida A, Tanaka M (2016) Two types of neurons in the primate globus pallidus external segment play distinct roles in antisaccade generation. *Cereb Cortex* 26:1187–1199. [CrossRef Medline](#)
- Zaragoza R, Budzik GP, Dillon TP, Opgenorth TJ (1992) Effect of cell density on endothelin release from endothelial cells and phosphoramidon dependent inhibition. *Biochem Pharmacol* 44:851–856. [CrossRef Medline](#)